

WIP1 is a conserved mediator of right ventricular failure

Christos Tzimas, ... , Yibin Wang, Emily J. Tsai

JCI Insight. 2019. <https://doi.org/10.1172/jci.insight.122929>.

Research In-Press Preview Cardiology

Right ventricular dysfunction is highly prevalent across cardiopulmonary diseases and independently predicts death in both heart failure (HF) and pulmonary hypertension (PH). Progression towards right ventricular failure (RVF) can occur in spite of optimal medical treatment of HF or PH, highlighting current insufficient understanding of RVF molecular pathophysiology. To identify molecular mechanisms that may distinctly underlie RVF, we investigated the cardiac ventricular transcriptome of advanced HF patients, with and without RVF. Using an integrated systems genomic and functional biology approach, we identified an RVF-specific gene module, for which *WIP1* served as a hub and *HSPB6* and *MAP4* as drivers, and confirmed the ventricular specificity of *Wipi1*, *Hspb6*, and *Map4* transcriptional changes in adult murine models of pressure overload induced RV- versus LV- failure. We uncovered a shift towards non-canonical autophagy in the failing RV that correlated with RV-specific *Wipi1* upregulation. In vitro siRNA silencing of *Wipi1* in neonatal rat ventricular myocytes limited non-canonical autophagy and blunted aldosterone-induced mitochondrial superoxide levels. Our findings suggest that *Wipi1* regulates mitochondrial oxidative signaling and non-canonical autophagy in cardiac myocytes. Together with our human transcriptomic analysis and corroborating studies in an RVF mouse model, these data render *Wipi1* a potential target for RV-directed HF therapy.

Find the latest version:

<https://jci.me/122929/pdf>



Title: *WIP1* is a conserved mediator of right ventricular failure

Authors: Christos Tzimas¹, Christoph D. Rau², Petra E. Buergisser¹, Gaston Jean-Louis Jr.¹, Katherine Lee^{1,3}, Jeffrey Chukwuneke¹, Wen Dun¹, Yibin Wang², Emily J. Tsai^{1,4,*†}

Affiliations:

¹ Division of Cardiology, Department of Medicine, Columbia University Vagelos College of Physicians and Surgeons, New York, NY 10032, USA.

² Division of Molecular Medicine, Department of Anesthesiology and Perioperative Medicine, David Geffen School of Medicine, UCLA, Los Angeles, CA 90095, USA.

³ Institute of Human Nutrition, Columbia University Vagelos College of Physicians and Surgeons, New York, NY 10032, USA.

⁴ Cardiovascular Research Center, Lewis Katz School of Medicine, Temple University, Philadelphia, PA 19140, USA.

*To whom correspondence should be addressed:

Emily J. Tsai, MD

630 W. 168th Street, P&S 8-510, New York, NY 10032

Phone: (212) 305-3409

E-mail: emily.tsai@columbia.edu

†Current address: Columbia University Vagelos College of Physicians and Surgeons, New York, NY 10032, USA.

Conflict of Interest: EJT and CT have filed a provisional patent (#62/755,106) on pharmacological treatment for right ventricular failure.

Abstract: Right ventricular dysfunction is highly prevalent across cardiopulmonary diseases and independently predicts death in both heart failure (HF) and pulmonary hypertension (PH). Progression towards right ventricular failure (RVF) can occur in spite of optimal medical treatment of HF or PH, highlighting current insufficient understanding of RVF molecular pathophysiology. To identify molecular mechanisms that may distinctly underlie RVF, we investigated the cardiac ventricular transcriptome of advanced HF patients, with and without RVF. Using an integrated systems genomic and functional biology approach, we identified an RVF-specific gene module, for which *WIP1* served as a hub and *HSPB6* and *MAP4* as drivers, and confirmed the ventricular specificity of *Wipi1*, *Hspb6*, and *Map4* transcriptional changes in adult murine models of pressure overload induced RV- versus LV- failure. We uncovered a shift towards non-canonical autophagy, in the failing RV that correlated with RV-specific *Wipi1* upregulation. *In vitro* siRNA silencing of *Wipi1* in neonatal rat ventricular myocytes limited non-canonical autophagy and blunted aldosterone-induced mitochondrial superoxide levels. Our findings suggest that *Wipi1* regulates mitochondrial oxidative signaling and non-canonical autophagy in cardiac myocytes. Together with our human transcriptomic analysis and corroborating studies in an RVF mouse model, these data render *Wipi1* a potential target for RV-directed HF therapy.

INTRODUCTION

Right ventricular dysfunction (RVD) predicts worse clinical outcomes, including death, in heart failure (HF) (1-6) and pulmonary hypertension (PH) patients (7-9), irrespective of etiology, left ventricular function, or pulmonary artery pressures. Although RVD is largely a consequence of pulmonary hypertension, left heart disease is the most common etiology of PH, and HF patients with RVD outnumber other PH patients with RVD. More than half of all HF patients are estimated to have RVD--- 25-50% of HF patients with preserved left ventricular ejection fraction (HFpEF) and up to 75% of those with reduced left ventricular ejection fraction (HFrEF) (5, 10, 11). Strikingly, current guideline directed HF pharmacotherapies neither reverse RVD nor prevent RV failure (RVF) (12). This discrepancy should not be surprising. The right ventricle is distinct from the left ventricle with regards to embryological origin, morphology, physiology, and response to stress. Diuretics, inotropic medications, and, in select cases, advanced pulmonary vasodilators are empiric medications used for managing RVF. However, none of these improve long term outcomes in HF patients, and there remain no RV-targeted therapies for either PH or HF patients.

To date, efforts in drug development for PH and HF have focused, respectively, on pulmonary vascular remodeling and LV function, not RV function directly. Preclinical studies have been challenged by limitations of commonly used animal models that were developed to study pulmonary vascular disease rather than RV dysfunction or biventricular HF. Some studies have sought to identify molecular signatures of RVF, using animal models (13-17) or human tissue (18-20). Most of these were limited to animal models or patients with RV dysfunction but not RV failure (13, 14, 16, 18, 19). These prior studies did not pursue experimental validation or mechanistic studies of their potential molecular signatures of RV dysfunction (13-20). All relied

upon biased pathway analyses of select differentially expressed genes. Although widely used, pathway analyses are limited by an emphasis on individual genes, the resolution of the associated knowledge base, potentially incorrect and inaccurate annotations, and lack of dynamic information (21).

Here, we sought to analyze the ventricular transcriptome of advanced HF patients, with versus without hemodynamically significant RVF, to identify gene networks that may be uniquely altered in RVF. We integrated weighted gene co-expression network analysis (WGCNA) with detailed hemodynamic indices of advanced HF patients to identify a gene network (module) that correlated specifically with RVF. By validating gene hubs and drivers of this network in murine HF models, we identified *Wip1* as a conserved mediator of RVF. Furthermore, silencing *Wip1* in aldosterone-stimulated, isolated neonatal rat cardiac myocytes blunted excessive non-canonical autophagy and mitochondrial superoxide levels, suggesting *Wip1* as a potential target for therapeutic intervention.

RESULTS

Clinical and hemodynamic characteristics of advanced heart failure patients

Clinical characteristics of advanced HFrEF patients without RVF and thereby with LV failure alone (LV-HF), advanced HFrEF patients with RVF and thereby biventricular failure (BiV-HF), and non-failing (NF) adult patients are listed in Supplemental Table S1. The median (interquartile range) age was 61.5 (60.0-63.5) yrs for all advanced HF patients and 51.0 (43.0-52.0) yrs for non-failing donors. There was no significant difference in age between LV-HF and BiV-HF patients. As would be expected, BiV-HF patients had higher rates of inotropic medication use, lower rates of β -blocker use, lower LVEF, and worse hemodynamic indices of RV function than LV-HF patients (Supplemental Tables S1, S2). Specifically, BiV-HF patients had markedly elevated right atrial pressure (RAP), increased ratio of right atrial pressure to pulmonary capillary wedge pressure (RA:PCWP), lower systolic and mean arterial blood pressure (SBP and MAP), markedly decreased ratio of mean arterial pressure to right atrial pressure (MAP:RA), and lower cardiac index (CI) in spite of greater inotropic support.

Transcriptomic analysis identifies a gene module uniquely associated with RVF

We used WGCNA to identify genetic pathways and groups of genes that distinguish the RV from the whole heart (22). Using only genes that were expressed (average FPKM>1) and variable (coefficient of variation >10% across all cohorts) in the RV, we partitioned 13,613 transcripts into 23 RV-derived gene modules. Each module was defined by a tighter clustering coefficient compared to the network as a whole. We examined the correlation of the eigengene for each of the 23 RV-derived network modules with hemodynamic indices of RVF.

Consequently, we identified one module that correlated significantly with elevated RAP, elevated RA:PCWP, decreased SBP, and decreased CI (Supplemental Figure S1). This RV-

derived, RVF-associated module contained 279 transcripts, of which 245 were protein-coding genes, 30 were novel transcripts, and 4 were non-coding RNAs (1 long intergenic non-coding RNA, 1 pseudogene, 1 regulatory RNA, 1 anti-sense RNA). These 279 transcripts displayed an average of 6.9 connections per transcript (Figure 1). GeneAnalytics revealed that the module was enriched in genes involved in striated muscle contraction, cytoskeletal signaling, fMLP (N-formyl-Met-Leu-Phe) signaling, receptor tyrosine kinase EphB-EphrinB signaling, oxidative stress response, and protein metabolism (Supplemental Data File S1). Other signaling pathways already known to be involved in HF---- PKA signaling, PI3K-Akt signaling, Wnt signaling, and AMPK signaling--- were also highlighted. Strikingly, the RVF-associated module appeared trilobed in structure. Two of the three lobes had strong, distinct physiological themes--- muscle filament sliding and striated muscle contraction (cardiac signaling lobe, Supplemental Data File S2); and neutrophil degranulation and innate immune system signaling (innate immunity signaling lobe, Supplemental Data File S3). The cardiac signaling lobe was also enriched in genes involved in cytoskeletal signaling, cell death (apoptosis and autophagy), and intracellular membrane transport. The innate immune system signaling lobe was additionally enriched in genes involved in cytokine signaling, cell chemotaxis, and PLC signaling. The third lobe of the RVF-associated module was moderately enriched in genes involved in Notch signaling, fMLP pathway, metabolism, calcium homeostasis, and ER stress (intracellular signaling lobe, Supplemental Data File S4).

WIPI1, HSPB6, MAP4, SNAP47, and PRDX5 are potential determinants of RVF

To elucidate the mechanisms by which the RVF-associated module may regulate RV failure, we focused on a) those genes with high connectivity to other genes (“hubs”) and b) those with high positive or negative correlations to hemodynamic indices of RVF (“drivers” or “repressors”). Of

the 10 hubs, only *WIP1I* encoding autophagy and mitophagy WD repeat domain phosphoinositide interacting protein 1 was: a) differentially expressed in RV of BiV-HF hearts versus the RV of either LV-HF or NF hearts; and b) differentially expressed in RV versus LV of BiV-HF hearts (Supplemental Table S3). Moreover, the expression of *WIP1I* correlated with multiple RVF-associated hemodynamic indices (Table 1).

To identify genetic drivers and repressors of RVF, we examined the correlation of each of the 279 transcripts within the RVF-associated module to RAP, RA:PCWP, MAP:RA, PASP, SBP, and CI (Supplemental Data File S5). Increased *HSPB6*, *SNAP47* and *MAP4* expression and decreased *PRDX5* expression were associated with increased RAP, PASP, and RA:PCWP and with decreased MAP:RA, SBP, and CI--- consistent with RVF (Table 1).

Wipi1, Hspb6, and Map4 are upregulated only in the failing RV and not in the merely dysfunctional RV

To validate their associations with RVF, we measured the ventricular expression of *Wipi1*, *Hspb6*, *Snap47*, *Map4*, and *Prdx5* in a mouse model of pressure overload induced RVF. Adult male C57BL/6J mice (age 10-12 wk) were subjected to moderate pulmonary artery banding (PAB, 25g) or thoracotomy alone (Sham) and assessed at 3-wk intervals following surgery. By 3 wk post-PAB, RV systolic dysfunction and mild RV dilatation were echocardiographically evident (Figure 2A-D). However, RV failure, defined as markedly elevated RV end-diastolic pressure, diminished RV stroke volume, and pathological evidence of elevated central venous pressure in the form of hepatic congestion (increased liver weight/tibia length), did not manifest until 9 wk post-PAB (Figure 2E, F). By 9 wk post-surgery, PAB mice also developed mild pulmonary edema (increased lung weight/tibia length) and peripheral edema (increased BW/tibia length). Failing PAB9wk mice also demonstrated marked induction of the fetal gene program,

namely upregulation of atrial natriuretic factor (*Nppa*), brain natriuretic peptide (*Nppb*), and skeletal alpha actin (*Acta1*), and switching of cardiac myosin heavy chain isoforms to a predominance of β MHC, encoded by *Myhc7* (Figure 2G).

As in the human BiV-HF hearts, *Wipi1*, *Hspb6*, *Snap47*, and *Map4* mRNA expression were increased in the failing RV of PAB mice (PAB9wk-RV) compared to that of time-matched Sham (Sham9wk-RV) (Figure 3A). Transcriptional analyses at 3- and 6- wk post-surgery confirmed that *Wipi1*, *Hspb6*, and *Map4* inductions were indeed specific to RVF (PAB9wk) and not associated with simply RV pressure overload or RV dysfunction. Western analysis confirmed increased protein expression at PAB9wk of WIP1, HSPB6, and MAP4 but not SNAP47 (Figure 3B-C). In contrast to the findings in human BiV-HF RV, there was no difference in *Prdx5* expression between PAB9wk-RV and Sham9wk-RV, at either the transcript or protein level.

Transcriptional upregulation of Wipi1, Hspb6, and Map4 are specific to the failing RV and not evidenced in the failing LV

To confirm that these transcriptional changes were specific to the failing RV and not shared by the failing LV, we also assessed the expression of these gene hub and drivers/repressors in a mouse model of pressure overload induced LVF (Supplemental Figure S2). Adult male C57BL/6J mice (age 10-12 wk) were subjected to severe transverse aortic constriction (TAC, 27g) or Sham and assessed at 3-wk intervals following surgery. By 3 wk post-surgery, TAC mice developed increased LV mass and depressed LV systolic function. By 6 wk post-surgery, TAC mice progressed to severe LV dysfunction, LV dilatation, and overt LVF, as manifested by severe pulmonary edema on terminal morphometric analysis; induction of the fetal gene program was also confirmed. Expression of *Wipi1*, *Hspb6*, *Snap47*, *Map4*, and *Prdx5* in the failing LV of TAC6wk mice were similar to that in LV of Sham6wk mice.

In vitro silencing of Wipi1 partially protects against RVF-associated neurohormone-induced HF

WGCNA discovered modest to strong correlations between RVF-associated hub *WIP1* and each of our candidate RVF-associated drivers and repressors, suggesting potential functional or biological interactions between them (*MAP4* $R^2=0.802$, *SNAP47* $R^2=0.726$, *HSPB6* $R^2=0.672$, and *PRDX5* $R^2=0.608$.) Our in vivo RVF mouse model validated that transcriptional changes in *Wipi1* correlated with that of *Hspb6* and *Map4*, thereby raising the hypothesis that *Wipi1* might potentially regulate one or both of these RVF-associated drivers. As a genetic hub of RVF, *Wipi1* may be a potential target for RVF therapy. Thus, we sought to ascertain the cardioprotective potential of silencing *Wipi1* in an in vitro model of heart failure and its effect on RVF-associated drivers. Specifically, we cultured isolated neonatal rat ventricular myocytes (NRVMs) with aldosterone to mimic the neurohormonal activation predominantly associated with RV dysfunction and failure (23-26). In control NRVMs transfected with non-targeting siRNA (si-scramble), neurohormonal stimulation with aldosterone significantly increased the expression of *Nppa*, *Nppb*, *Acta1*, and *Myh7*, consistent with induction of the fetal gene program in heart failure (Supplemental Figure S2). Specific siRNA (si-*Wipi1*) significantly knocked down *Wipi1* expression in NRVMs by ~70% at both the mRNA and protein levels (Figure 4). Notably, silencing *Wipi1* prevented aldosterone-induced upregulation of *Myh7*, suggesting that silencing *Wipi1* may be partially protective against the neurohormone-activation associated with RVF (Supplemental Figure S3).

Wipi1 regulates Map4 expression under conditions of aldosterone activation

To determine whether RVF hub *Wipi1* might regulate *Hspb6*, *Map4*, *Snap47*, and/or *Prdx5*, we also assessed the mRNA and protein expression of these genes in si-*Wipi1* versus si-scramble

transfected NRVMs. The effect of silencing *Wipi1* on *Map4*, *Hspb6*, *Snap47*, and *Prdx5* varied. Silencing *Wipi1* in NRVMs decreased *Map4* transcript expression by 25-30% relative to its expression in si-scramble control NRVMs, under both basal and aldosterone stimulated conditions (Figure 4A, B). Aldosterone did not affect *Map4* transcript levels in either si-*Wipi1* or si-scramble NRVMs. However, aldosterone did induce MAP4 protein expression in si-scramble control NRVMs. This aldosterone-induced upregulation of MAP4 protein expression was not observed in si-*Wipi1* NRVMs (Figure 4C). In contrast, silencing *Wipi1* had no impact on *Hspb6* transcript expression. Aldosterone stimulated *Hspb6* transcript expression in both si-*Wipi1* and si-scramble NRVMs. HSPB6 protein expression was consistent with transcript data. Neither silencing *Wipi1* nor stimulating with aldosterone affected *Snap47* or *Prdx5* transcript or protein expression. Taken together, our findings validated the WGCNA calculated correlation between *Wipi1* and *Map4* transcripts.

Wipi1 upregulation correlates with increased non-canonical autophagy in the failing RV

Since WIPI1 has been implicated in early autophagosome formation (27, 28), we investigated whether autophagy might be differentially dysregulated in the failing RV versus the failing LV. An autophagy-focused heat map of our human ventricular transcriptomic data suggested differential dysregulation of autophagy pathways in the failing RV versus the failing LV (Supplemental Figure S4). To substantiate this hypothesis, we sought to characterize autophagy in our mouse models of RV versus LV failure. We analyzed the expression of autophagy proteins beclin-1 (BECN1) and microtubule-associated protein light-chain 3 (LC3), the ratio of the phosphatidylethanolamine conjugate to the cytosolic isoform of LC3 (LC3-II/I) as an index of LC3-lipidation and autophagic flux (29), and serine 16-phosphorylation of heat shock protein B6 (HSPB6) as a marker of canonical autophagy (30) (Figure 5A). BECN1, HSPB6, WIPI1, and

LC3I were all upregulated in PAB9wk-RV compared to Sham9wk-RV (Figure 5B). However, LC3II expression and LC3-II/I ratio remained similar in PAB9wk-RV and Sham9wk-RV. Coupled with the finding that Ser16-phosphorylated-/total- HSPB6 ratio remained low and unchanged in PAB9wk-RV relative to Sham9wk-RV (Figure 5C), these findings suggest that in the failing RV, non-canonical autophagy is upregulated while canonical autophagy is not. In contrast, in the failing TAC6wk-LV, both HSPB6 and its Ser16 phosphorylation were increased relative to levels in Sham6wk-LV (Supplemental Figure S5), suggesting an upregulation of canonical autophagy in the failing LV. Hence, non-canonical autophagy may play a more significant role in the pathophysiology of RVF, while phospho-Ser16 HSPB6-mediated, BECN1-dependent, canonical autophagy is more predominant in LVF.

*Silencing *Wipi1* prevents aldosterone-induced non-canonical autophagy in NRVMs*

Given the central role for WIPI1 across multiple autophagy pathways (31, 32) and our finding of increased non-canonical autophagy in the RVF mouse model, we hypothesized that silencing *Wipi1* might restore a physiological balance of autophagy pathways by blunting the excessive non-canonical autophagy associated with RVF. We assessed the effect of silencing *Wipi1* upon BECN1 expression, LC3 lipidation, and Ser16-phosphorylation of HSPB6 in our in vitro model of RVF-associated neurohormone activation. Isolated NRVMs were transfected with either si-scramble or si-*Wipi1* and subsequently cultured for 48h, under serum starved conditions, with or without aldosterone. In si-scramble control NRVMs, aldosterone did not affect BECN1 expression or LC3-lipidation but did decrease Ser16-HSPB6 phosphorylation in si-scramble NRVMs (Figure 6A, B). These results suggest that aldosterone inhibits pSer16-HSPB6/BECN1-dependent (canonical) autophagy while increasing non-canonical autophagy in cardiac myocytes for a net constant overall autophagic flux. Under basal conditions, silencing *Wipi1* had no affect

on BECN1 expression, LC3 lipidation, or Ser16-HSPB6 phosphorylation. However, under aldosterone stimulation, silencing *Wipi1* decreased LC3-lipidation (LC3II/I ratio) without affecting Ser16-HSPB6 phosphorylation relative to the respective si-scramble control. Hence, silencing *Wipi1* could selectively limit non-canonical autophagy under conditions of chronic aldosterone activation.

To further elucidate the role of WIPI1 in canonical versus non-canonical autophagy, we used two distinct autophagy inhibitors to differentiate the effects of *Wipi1* silencing on these autophagy pathways. V-ATPase inhibitor bafilomycin A (BafA) blocks LC3II lysosomal degradation during canonical autophagy. Chloroquine (CQ) inhibits the fusion between the autophagosome and lysosome, thereby rendering it capable of revealing total autophagic flux, inclusive of both canonical and non-canonical autophagy (33, 34). Thus, the difference between the effects of CQ versus BafA on LC3-II/I ratios is attributed to non-canonical autophagy. Here, we transfected NRVMs with si-*Wipi1* versus si-scramble, treated them with either BafA or CQ, and then measured LC3-II/I ratios (Figure 6C). BafA increased LC3-II/I equally in si-*Wipi1* and si-scramble transfected NRVMs, suggesting that canonical autophagy remains intact even when *Wipi1* is silenced. However, silencing *Wipi1* blunted CQ-induced increase of LC3-II/I otherwise seen in si-scramble transfected NRVMs (Figure 6D), suggesting that *Wipi1* plays a significant role in non-canonical autophagy.

Silencing Wipi1 blunts aldosterone induction of mitochondrial superoxide and mitochondrial protein oxidation

Recent studies have revealed an emerging relationship between mitochondrial oxidative stress and autophagy (35, 36). Thus, we investigated the effect of silencing *Wipi1* on mitochondrial superoxide levels in NRVMs subjected to aldosterone. Aldosterone increased mitochondrial

superoxide levels in si-scramble control NRVMs as observed with the MitoSOX Red superoxide indicator (Figure 7A, B). Silencing *Wipi1* blunted aldosterone-induced mitochondrial superoxide but not that induced by hydrogen peroxide (H_2O_2). Neither aldosterone stimulation nor silencing *Wipi1* negatively impacted cell viability (Figure 7C). Moreover, subsequent assessment of the redox state of mitochondrial proteins cyclophilin D (CYPD) and thioredoxin 2 (TRX2) confirmed that silencing *Wipi1* prevents downstream oxidation of these mitochondrial proteins (Figure 8). Silencing *Wipi1* blunted aldosterone-induced oxidation of CYPD and TRX2 but had no effect on H_2O_2 -induced protein oxidation (Figure 8B-D). Altogether, these results indicate that silencing *Wipi1* not only protects cardiac myocytes from excessive non-canonical autophagy but also mitigates mitochondrial oxidative stress by blunting mitochondrial superoxide levels and limiting mitochondrial protein oxidation.

DISCUSSION

Right ventricular failure portends accelerated clinical decline and early death in patients with cardiac or pulmonary disease, and yet no therapies exist that directly target the RV. The goal of this study was to leverage human transcriptomic data to identify myocardial determinants of RV failure and experimentally validate candidate genes in *in vivo* and *in vitro* models of RVF. Using an unbiased and robust, large-scale, module-based statistical approach, we identified *WIP11* as a genetic hub of RVF, experimentally validated it in mouse models, and tested hypotheses regarding its pathophysiological role in isolated cardiac myocytes under conditions mimicking the neurohormonal activation of RVF. We provide new insights into the role of *Wipi1* in non-canonical autophagy and in mitochondrial oxidative stress signaling. Our findings also offer proof of principle that silencing cardiac myocyte *Wipi1* signaling holds therapeutic potential in RV failure, by preventing excessive non-canonical autophagy and blunting mitochondrial superoxide levels and mitochondrial protein oxidation (Figure 9).

WIP11 was first discovered for its role in nascent autophagosome formation and subsequently implicated in both canonical and non-canonical autophagy pathways (37). Although cardiac myocyte autophagy has been associated with human heart failure (38, 39), the precise roles of canonical versus non-canonical autophagy in cardiovascular disease is unknown and unexplored. Transgenic mice with gain or loss of function of autophagy related genes (40-43) and animal models of induced cardiac dysfunction (30, 35, 40, 41, 43-46) have demonstrated both cytoprotective and pathologic roles of autophagy in the heart. Moreover, both increased and decreased autophagic flux have been associated with LV failure. Such ambiguity might be explained by differential dysregulation of canonical versus non-canonical autophagy (31). Whereas canonical autophagosome formation involves distinct hierarchical steps that require

specific ATG (autophagy-related) proteins at each stage, non-canonical autophagosome formation does not require the involvement of all ATG proteins. Non-canonical autophagosome elongation may also occur from multiple membrane sources or from pre-existing, non-phagophore endomembrane. Notably, non-canonical autophagy pathways include those that are independent of either BECN1 or LC3-lipidation. Prior cardiac autophagy studies often assessed autophagic flux via LC3-lipidation, a step universal to canonical and some non-canonical autophagy pathways as well as mitophagy, but did so without distinguishing these pathways. Both canonical and non-canonical autophagy are likely important for cellular homeostasis, and dysregulation of either or both pathways may underlie specific pathophysiological responses.

By incorporating analyses of a recently identified upstream regulator of canonical autophagy (*i.e.* phospho-Ser16 HSPB6) with that of LC3-lipidation, we provide original evidence suggesting that increased non-canonical autophagy distinguishes the failing RV from the failing LV. Furthermore, we demonstrated in NRVMs that silencing *Wipi1* can limit aldosterone-induced non-canonical autophagy while still permitting canonical autophagy. Our finding is significant as it provides evidence that these autophagy pathways can be differentially intervened upon under pathological conditions. Further studies are needed to elucidate the differential role of WIPI1 in non-canonical versus canonical autophagy.

Strikingly, our studies also suggest novel functions for WIPI1. We provide evidence that WIPI1 regulates mitochondrial oxidative stress signaling. Silencing *Wipi1* in NRVMs decreased aldosterone-stimulated mitochondrial superoxide levels and limited oxidation of mitochondrial proteins CYPD and TRX2. The significance of this discovery is two-fold. First, the RV is more vulnerable than the LV to oxidative stress due to interventricular differences in ROS regulation (47). Thus, attenuating mitochondrial oxidative stress, either through decreasing mitochondrial

ROS production or improving antioxidant defense, is a promising therapeutic approach for RVF. Secondly, autophagy is known to regulate redox homeostasis; intracellular ROS triggers autophagy and mitophagy, which in turn modulate ROS levels. Dysregulated autophagy may potentiate detrimental ROS signaling. WIPI1 appears to lie at the nexus of autophagy and mitochondrial ROS signaling. How exactly WIPI1 regulates mitochondrial superoxide surpasses the scope of our current study but warrants further investigation.

Another novel function of WIPI1 proposed by our studies relates to its observed correlation with MAP4 (microtubule associated protein 4). WGCNA of human ventricular tissue revealed a strong correlation between *WIPI1* and *MAP4*, which we then corroborated in our mouse model of RVF. We subsequently found that silencing *Wipi1* in NRVMs reduced *Map4* transcript levels, at baseline and with aldosterone stimulation. MAP4 protein expression data in the NRVMs was not as definitive; MAP4 protein levels did not mirror all the changes observed at the transcript level, perhaps reflecting differential kinetics in mRNA translation or protein degradation at baseline versus neurohormonal activation. Nevertheless, aldosterone induced MAP4 protein expression in si-Scramble NRVMs but not in si-*Wipi1* NRVMs, suggesting that the correlation between *Wipi1* and *Map4* transcript expression is biologically significant. MAP4 is involved in microtubule stabilization (48, 49), myogenesis (50), myocyte metabolism (51), and inhibition of microtubule-based mRNA active transport (52). Overexpression of MAP4 in isolated cardiac myocytes and transgenic mice has been shown to cause cardiac myocyte contractile dysfunction (53). Our findings suggest that WIPI1 might regulate *Map4* transcription itself and, in doing so, could theoretically impact upon MAP4-mediated cellular processes.

Our identification of *HSPB6* as a driver of RV failure is consistent with current understanding of HSPB6 but also presents new insights. In our in vitro and in vivo RVF models,

HSPB6 was upregulated but its phosphorylation was not. Phosphorylated HSPB6 plays important roles in cardiac contractile function (54-56), canonical autophagy(30, 57), and cardioprotection(30, 58). Increased cardiac expression of phosphorylated HSPB6 has been reported in the LV of advanced HFrEF patients (30), suggesting excessive canonical autophagy in the failing LV. Our finding of increased Ser16 phosphorylation of HSPB6 in the failing LV of TAC mice is consistent with this human data. Whether non-phosphorylated HSPB6 has distinct pathophysiological actions or reflects deficiencies in processes otherwise mediated by phosphorylated HSPB6 remains unclear. Our findings suggest differences between the failing RV and the failing LV with regards to HSPB6 signaling and autophagy pathways.

Above all, our study stands out for its unbiased, comprehensive approach to identifying molecular pathophysiological signaling specific to the failing RV. Prior transcriptomic analyses of animal models and human tissue have relied upon differential-expression and pathway analyses without subsequent experimental and mechanistic validation studies of proposed molecular signatures of RVF (13-20). Although single-gene and differential-expression analyses are powerful tools, there are a number of advantages with WGCNA (59). As a module-based approach, WGCNA is well-suited to analyze large datasets and to take a more global view. Moreover, by examining the interaction patterns between genes to identify gene modules (networks), WGCNA filters results to a meaningful subset of the total expression data in an unsupervised, unbiased manner. WGCNA is also able to utilize and incorporate subtle shifts in gene expression, making it better able to elucidate true changes in samples compared to differential expression approaches. By correlating these modules to hemodynamic indices of RVF, we discovered a robust, biologically significant and interesting gene network. With WGCNA, we could leverage betweenness centrality to identify important actors in the alteration

of a phenotype whereas such an analysis is impossible in a list of differentially expressed genes. Further investigation of intramodular connectivity between genes allowed us to identify key genetic drivers or hubs that could be experimentally validated, targeted for therapeutics, or used as novel biomarkers. Additionally, WGCNA can link novel with known genes, thereby assisting in the identification of potential functions and biological processes of novel genes. For example, WGCNA has been instrumental in identifying genetic programs critical to embryonic development (60) and cardiac myocyte differentiation (61). Finally, since WGCNA is expression rather than interaction-based, it is better able to identify large, high-impact modules driven by changes due to transcription factors and other global signaling processes as compared to an interaction-based network which excels at the exact recreation of already known pathways.

Limitations

Despite its robustness for understanding global patterns that underlie phenotypic traits, WGCNA does have some limitations. Firstly, as a statistically-driven method, WGCNA may link genes that are not involved in the exact same molecular pathway. Instead, linked genes may represent related but non-interacting members of two parallel processes. Thus, experimental validation is absolutely necessary. Secondly, the WGCNA algorithm may distort the true relationships between genes and phenotypes through the use of the soft thresholding algorithm. The soft thresholding algorithm alters expressed genes by raising them to an algorithm-guided power and uses only the first principle component of a module, which may represent only a small fraction of the total variance of a module, as a proxy measure for correlation between a phenotype and the entire module. Our first principle component accounted for 77% of the total variance (Supplemental Fig. S6), suggesting that these concerns do not apply to our data. Thirdly, the algorithm used by Cytoscape to generate betweenness centralities is incapable of

working with weighted edges. A weighted betweenness centrality approach may be able to more accurately identify hub genes. Lastly, because our modules are derived computationally, hubs which physically interact with many genes but which do not affect their expression will not be observed in our results. Despite these limitations, WGCNA and module-phenotype analyses still offer biologically significant insights that simply cannot be afforded by single-gene and differential-expression analyses. Importantly, these limitations of WGCNA can be addressed through experimental validation and testing, as we have done.

In vitro modeling of RV failure is particularly challenging compared to that of LV failure. Morphologic and physiologic differences between the RV and LV as well as those between the pulmonary and systemic vasculatures profoundly magnify the pathophysiologic role of increased arterial elastance (decreased pulmonary vascular compliance) in RV failure (62). As suggested by our mouse model, chronicity of both pressure overload and neurohormonal activation are likely important determinants of *Wipi1* expression. Thus limitations inherent to in vitro cell culture models might explain why *Wipi1* transcript and protein expression were upregulated in the failing RV of PAB mice but not in aldosterone-stimulated NRVMs. Despite this discrepancy, our in vitro studies with si-*Wipi1* still revealed a significant functional role of *Wipi1* in mediating aldosterone-induced mitochondrial superoxide levels. Importantly, others have already demonstrated that hyperaldosteronism is associated with RV failure in large animal models(23) and patients (26). Moreover, mitochondrial ROS play a significant role in the pathophysiology of RV failure but not that of LV failure (63).

Our experimental data regarding the cardioprotective effect of silencing *Wipi1* is limited to in vitro studies at this time. Silencing *Wipi1* had the greatest effects on aldosterone-induced mitochondrial superoxide signaling and non-canonical autophagy but only a small impact on the

fetal gene program. This highlights the limitation of using the fetal gene program as a surrogate outcome for RV failure, rather than necessarily a limitation of the therapeutic potential of targeting *Wipi1*. Given the known pathophysiological roles of aldosterone and mitochondrial ROS in RV failure, the substantial blunting of aldosterone-induced mitochondrial superoxide levels and mitochondrial protein oxidation by si-*Wipi1* is particularly significant. In vivo studies are needed to confirm the therapeutic potential of silencing or inhibiting *Wipi1* in RV failure.

Conclusions

In summary, our data demonstrate novel roles for *WIP11* in regulating mitochondrial oxidative stress signaling, non-canonical autophagy, and MAP4 transcription in RV failure. Silencing *Wipi1* in an in vitro model of RVF-associated neurohormone activation decreased mitochondrial superoxide levels and mitochondrial protein oxidation, dampened excessive non-canonical autophagy, and reduced *Map4* mRNA expression. Given the significance of RV dysfunction and failure and the absence of RV-targeted therapies, further investigation into how *WIP11* mediates these processes is warranted and may lead to innovative therapies for RV failure.

MATERIALS AND METHODS

Study Design

The goal of this study was to identify unique genetic determinants of RV failure that might be targeted for the development of novel RVF-specific therapy. Towards this end, we leveraged transcriptomic data from human ventricular tissue of advanced HF patients with versus without hemodynamically significant RVF as well as that from non-failing donors (n=5 patients per group). Using WGCNA, module-trait analysis, and subsequent gene-phenotype correlations, we identified genes likely to mediate RVF. We experimentally validated some of the candidate RVF-associated genes in mouse models of pressure-overload induced RV versus LV failure. We subsequently focused our attention on the genetic hub *WIP11* which was upregulated in the failing RV of HF patients and mouse models and also correlated with other identified RVF-associated genetic drivers. To elucidate possible pathophysiological mechanism of *WIP11* and test its potential as a therapeutic target, we performed *in vitro* isolated cardiac myocyte cell culture studies, in which cells were subjected to neurohormonal activation associated with RVF, namely aldosterone activation. We silenced *Wip11* in this *in vitro* model and assessed the effect on autophagy, mitochondrial superoxide levels, and the fetal gene program associated with HF. Supplemental Methods are available online.

Human ventricular tissue samples

Human ventricular myocardium was obtained from end-stage ischemic cardiomyopathic hearts explanted at the time of cardiac transplantation, as previously described (64). Non-failing donor hearts that were unsuitable for transplantation were used as control.

RNAseq

End-stage ischemic cardiomyopathic hearts were selected for RNA sequencing based upon patient's invasive hemodynamic parameters prior to transplantation and the absence of left ventricular assist device as a bridge to transplantation. The LV-HF cohort, defined as those without hemodynamic evidence of RVF, were selected based upon $RA < 8\text{mmHg}$ and $RA:PCWP < 0.5$. The BiV-HF cohort, defined as those with hemodynamic evidence of RVF and thereby biventricular HF, were selected based upon $RA > 15\text{mmHg}$ and $RA:PCWP > 0.62$. These hemodynamic criteria for RVF were based upon prior studies establishing cutoff values for $RA(65)$ and $RA:PCWP(2)$ in advanced HF patients. Only matched LV and RV tissue (from the same patient) were used. RNA extraction was performed with a Total RNA Purification Plus Micro Kit (Norgen Biotek). RNA sequencing was performed by LC Sciences (Houston, TX) with the Illumina platform. The RNA-Seq data from this publication have been submitted to the Gene Expression Omnibus (GEO) database (accession number GSE120852).

WGCNA

Networks were generated as previously described (22) using the parameters provided on-line (<http://labs.genetics.ucla.edu/horvath/htdocs/CoexpressionNetwork/Rpackages/WGCNA/Tutorials/>). The WGCNA method was implemented in the freely available WGCNA R package (22).

Module Selection and Enrichment

Eigengenes of the RV-only modules were correlated to RVF hemodynamic indices, and modules with significant correlations ($p < 0.05$) were further filtered to determine which RV modules were not preserved or weakly preserved in the combined network. This RV-specific, RVF-associated module was subsequently used to identify hubs and drivers. GeneAnalytics was used to identify

enriched biological categories in the genes of our modules of interest(66). Significance was determined by a Bejamini-Hochberg corrected binomial test $p < 0.05$.

Hubs

Betweenness centrality was calculated for each transcript using the NetworkAnalyzer tool in Cytoscape (67). Transcripts with significant betweenness centralities ('Hubs') have increased importance to overall modular structure. Significance was calculated by bootstrapping 100,000 networks with the same number of nodes and preserved degree structure using the `degree.sequence.game` function from the R package `igraph` (68) and an overall significance threshold (0.00029) determined by Bonferroni correction.

Drivers and Repressors

Drivers and repressors are genes connected to the rest of the module which respectively show strong independent positive or negative correlation with RVF hemodynamic indices. Genes with low betweenness centralities (lowest quartile) were removed. Genes significantly correlated to RVF hemodynamic indices were ranked based on p-value. Potential candidate drivers and repressors were selected based upon significant correlations, betweenness centrality, and previously validated expression in human cardiac tissue (69).

Module Visualization

Module visualization was performed using Cytoscape 3.4 (70). Node size reflected that node's betweenness centrality; node color reflected the transcript's correlation (direction and strength) to a composite RVF phenotype index averaging the correlation values of each transcript with RAP, PASP, and MAP:RA. The negative of the MAP:RA correlation value was used in this averaged index since MAP:RA is inversely related to RVF. Hence, drivers have positive

correlations to the RVF index, and repressors have negative correlations. Green node color indicates at least modest negative ($R^2 < -0.4$), yellow indicates minimal ($-0.4 \leq R^2 \leq 0.4$), and red indicating at least modest positive ($R^2 > 0.4$) phenotypic correlations. Module layout was determined via the “edge-weighted spring embedded” layout algorithm using the correlation strength between individual gene expressions as the edge weights. Edges with $R < 0.88$ were removed to aid visualization.

Heatmaps

Heatmaps were generated using the heatmap.2 function from the R package gplots (71).

RNA isolation and quantitative RT-PCR

Total RNA were extracted from animal tissues and cells using the Tissue RNA Purification Kit (Norgen Biotek) and the TRIzol reagent (Invitrogen) respectively, quantified using NanoDrop-2000c (Thermo Scientific), and reverse transcribed with iScript Supermix (Bio-Rad). qRT-qPCR was performed in triplicate using iTac Universal SYBR green Supermix (Bio-Rad) and the CFX96 Touch Detection System (Bio-Rad). Primer sequences are listed in Supplemental Table S4. Gene expression was normalized to *Rps13*, and relative mRNA expression was quantified using the $\Delta\Delta C_t$ method.

Protein isolation and Western blot analysis

Total protein were prepared from tissues and cells by homogenization in T-PER lysis buffer (Thermo Scientific) supplemented with the Halt Protease and Phosphatase Inhibitor Cocktail (Thermo Scientific) and quantified using BCA assay (Pierce). Protein samples were resolved on NuPAGE 4-12% Bis-Tris gradient gels (Invitrogen) and transferred to 0.2 μm nitrocellulose membranes (Bio-Rad). Membranes were stained with the LI-COR Revert Total Protein Stain kit

and analyzed. Membranes were subsequently blocked, incubated with primary antibodies at 4°C overnight, washed, and then incubated with the appropriate LI-COR secondary antibody.

ODYSSEY-Classic infrared imaging system (LI-COR) was used for quantitation. Target protein expression was normalized to total protein. Antibodies are listed in Supplemental Table S5.

Animal experiments

PAB, TAC, and Sham surgeries were performed as previously described (72, 73) with slight modifications.

Echocardiography

Mice were anesthetized with 1-2% inhalational isoflurane and transthoracic echocardiography was performed using a 18-38 MHz linear-array transducer probe with a digital ultrasound system (Vevo 2100 Image System, VisualSonics, Toronto, Canada). Vevo LAB 3.0 ultrasound analysis software (Fujifilm, VisualSonics) was used to measure and analyze images.

Hemodynamic assessment of RV function

A subset of PAB/Sham 6- and 9wk mice underwent terminal hemodynamic assessment, as previously described (74) but modified for the RV. RV cardiac catheterization was performed using a closed chest method whereby a Millar PVR-1035 (Millar Instruments, Houston, TX) mouse conductance catheter was inserted into the right external jugular vein and advanced into the RV. Upon hemodynamic stability, steady state baseline data were collected by the conductance catheter coupled to a Millar MPVS Ultra (Millar Instruments, Houston, TX) and PowerLab 16/35 data acquisition system (AD Instruments, Colorado Springs, CO). RV pressure and volume waveforms were recorded simultaneously and analyzed over a minimum of 10 consecutive cardiac cycles using LabChart 8 software (AD Instruments, Colorado Springs, CO).

Morphometric analysis

At experimental endpoint at 3, 6, or 9 wk following surgery, mice were euthanized and heparinized, and ventricles, lungs and liver were removed and weighed. Tissue weights were normalized to tibia length (TL) to assess pulmonary edema (lung weight/TL), hepatic congestion (liver weight/TL), and LV hypertrophy (LV/TL).

Isolation and primary culture of neonatal rat ventricular myocytes

Pregnant female Sprague-Dawley rats were purchased from Charles River Laboratories.

Neonatal Sprague-Dawley rats were euthanized by decapitation within the first 24h after birth and beating hearts were collected for digestion isolation of ventricular myocytes and single layer cell culture as previously described (75) with modifications.

siRNA transfection of NRVMs and in vitro model of neurohormone activation associated with RVF. At 24 h following isolation, NRVMs were transfected with 10 nM non-targeting siRNA (si-Scramble) or *Wip1*-targeting siRNA (si-*Wip1*) using Dharmafect #1 transfection reagent (Dharmacon). All siRNAs were ON-TARGETplus SMARTpool siRNAs (Dharmacon). Following 24 h transfection, cells were serum-starved in serum-free DMEM:F12 supplemented with penicillin (100 units/ml) / streptomycin (100 µg/ml) for 12h and then incubated with aldosterone (1µM) in serum-free DMEM:F12 culture medium for 48 h at 37°C, 5% CO₂. Serum-free DMEM:F12 culture medium without any aldosterone was used as a comparative control to neurohormone activation. For autophagy studies, transfected NRVMs were treated with either bafilomycinA1 (BafA, 100 nM) or chloroquine (CQ, 100 µM) for 1h prior to harvesting (33) in complete MEM medium.

MTT assay of cell viability

To assess NRVM viability, the Vybrant MTT cell proliferation assay kit was used (Molecular probes) according to manufacturer's protocol.

MitoSOX Red analysis

Mitochondrial superoxide level was monitored with the MitoSOX™ Red mitochondrial superoxide indicator (Molecular Probes) for live-cell imaging, according to manufacturer's instructions. Cells were imaged with a DMI8 fluorescent microscope (Leica) using a red fluorescent filter (excitation/emission 510/580 nm). Red fluorescent signal was measured with ImageJ software and normalized to brightfield signal.

Redox Western blots

In NRVMs, the redox state of the mitochondrial proteins CYPD and TRX2 was estimated by redox Western blot as previously described (76). Briefly, NRVMs were transfected with si-*Wip1* or si-scramble and incubated at 37°C under the following conditions: 1) non-treated control (18h); 2) N-Acetyl cysteine (NAC, 2 mM, 18h); 3) hydrogen peroxide (H₂O₂, 0.1 mM, 18h); and 4) aldosterone (Aldo, 1 μM, 48h). Cells were harvested and incubated in urea lysis buffer (8 M urea, 50 mM Tris/HCl (pH 8.3) and 1 mM EDTA) containing 20 mM iodoacetamide (IAM) to alkylate protein thiol groups. Protein was then cold acetone precipitated from the lysate supernatant, washed, then resuspended and incubated in urea lysis buffer containing 5 mM DTT to reduce the oxidized protein thiol groups. Subsequent incubation in 100 mM iodoacetic acid (IAA) in urea/DTT lysis buffer (final IAA concentration 50 mM) was performed to alkylate DTT-reduced thiol groups. Alkylation reactions were performed in the dark. Following the serial IAM/IAA alkylation, samples were subjected to urea-PAGE electrophoresis (7 M urea and 7.5% acrylamide) in non-reducing conditions and immunoblotted for CYPD and TRX2.

Statistical analyses

Statistical analyses of mouse and NRVM experiments were carried out using GraphPad Prism 8.0. Unless otherwise specified, data are expressed as mean \pm SEM. Means between two groups were compared using unpaired, two-tailed Student's t-test, unless otherwise specified. For redox Western blots, unpaired, one-tailed Student's t-test was used to determine whether the decrease in oxidized proteins seen with silencing *Wip1* was statistically significant. Here, we sought to detect change in just one direction. For multiple comparisons, one- or two-way ANOVAs were performed, followed by Tukey's multiple comparison tests. Statistical significance was defined as $p < 0.05$. For the assessment of RNA-seq data of each of the candidate WGCNA-identified RVF-associated genetic hub, drivers, and repressor, statistical significance was defined as $p < 0.10$, given the limited sample size, non-normal data distribution, and use of human tissue analysis as a discovery rather than validation approach.

Study approval

Patient consent, sample collection and preparation, and clinical data collection were performed according to a human subject research protocol approved by the IRB of the Lewis Katz School of Medicine at Temple University (PI: Tsai). Animal experiments were conducted in strict accordance with the recommendations in the Guide for the Care and Use of Laboratory Animal of the NIH. All animal protocols were approved by the IACUC of Columbia University.

Author contributions: CT designed, performed and analyzed all NRVM studies, conducted mouse research, contributed to manuscript writing, and created figures. CR performed the WGCNA and computational biology analysis, contributed to manuscript writing, and created figures. PEB supported NRVM studies and mouse research and their associated data analyses. GJL, JC, and KL supported the mouse research and associated data analysis. WD performed and analyzed mouse echocardiograms, morphometrics, and invasive hemodynamic measurements and contributed to manuscript writing and figure creation. YW provided critical revisions to the manuscript. EJT conceived the project, designed the research, performed mouse echocardiograms, analyzed data, wrote the manuscript, and contributed to figure creation.

Acknowledgments: We thank Q. Li (Columbia) for mouse surgical support and H. Chung (Columbia) for technical support. This work was supported in part by American Heart Association grant 15POST25310006 to CR; and NIH grants K08HL133706, R03HL109159, and R01HL138527 to EJT.

REFERENCES

1. Cenkerova K, Dubrava J, Pokorna V, Kaluzay J, and Jurkovicova O. Right ventricular systolic dysfunction and its prognostic value in heart failure with preserved ejection fraction. *Acta Cardiol.* 2015;70(4):387-93.
2. Drazner MH, Velez-Martinez M, Ayers CR, Reimold SC, Thibodeau JT, Mishkin JD, et al. Relationship of right- to left-sided ventricular filling pressures in advanced heart failure: insights from the ESCAPE trial. *Circ Heart Fail.* 2013;6(2):264-70.
3. Gerges M, Gerges C, Pistritto AM, Lang MB, Trip P, Jakowitsch J, et al. Pulmonary Hypertension in Heart Failure. Epidemiology, Right Ventricular Function, and Survival. *Am J Respir Crit Care Med.* 2015;192(10):1234-46.
4. Ghio S, Temporelli PL, Klersy C, Simioniuc A, Girardi B, Scelsi L, et al. Prognostic relevance of a non-invasive evaluation of right ventricular function and pulmonary artery pressure in patients with chronic heart failure. *Eur J Heart Fail.* 2013;15(4):408-14.
5. Gulati A, Ismail TF, Jabbour A, Alpendurada F, Guha K, Ismail NA, et al. The prevalence and prognostic significance of right ventricular systolic dysfunction in nonischemic dilated cardiomyopathy. *Circulation.* 2013;128(15):1623-33.
6. Peters A, Caroline M, Zhao H, Baldwin MR, Forfia PR, and Tsai EJ. Initial Right Ventricular Dysfunction Severity Identifies Severe Peripartum Cardiomyopathy Phenotype With Worse Early and Overall Outcomes: A 24-Year Cohort Study. *J Am Heart Assoc.* 2018;7(9).
7. Forfia PR, Fisher MR, Mathai SC, Houston-Harris T, Hemnes AR, Borlaug BA, et al. Tricuspid annular displacement predicts survival in pulmonary hypertension. *Am J Respir Crit Care Med.* 2006;174(9):1034-41.
8. Haddad F, Spruijt OA, Denault AY, Mercier O, Brunner N, Furman D, et al. Right Heart Score for Predicting Outcome in Idiopathic, Familial, or Drug- and Toxin-Associated Pulmonary Arterial Hypertension. *JACC Cardiovasc Imaging.* 2015;8(6):627-38.
9. van de Veerdonk MC, Kind T, Marcus JT, Mauritz GJ, Heymans MW, Bogaard HJ, et al. Progressive right ventricular dysfunction in patients with pulmonary arterial hypertension responding to therapy. *J Am Coll Cardiol.* 2011;58(24):2511-9.
10. Mohammed SF, Hussain I, AbouEzzeddine OF, Takahama H, Kwon SH, Forfia P, et al. Right ventricular function in heart failure with preserved ejection fraction: a community-based study. *Circulation.* 2014;130(25):2310-20.
11. Puwanant S, Priester TC, Mookadam F, Bruce CJ, Redfield MM, and Chandrasekaran K. Right ventricular function in patients with preserved and reduced ejection fraction heart failure. *Eur J Echocardiogr.* 2009;10(6):733-7.
12. Yancy CW, Jessup M, Bozkurt B, Butler J, Casey DE, Jr., Drazner MH, et al. 2013 ACCF/AHA guideline for the management of heart failure: executive summary: a report of the American College of Cardiology Foundation/American Heart Association Task Force on practice guidelines. *Circulation.* 2013;128(16):1810-52.
13. Drake JI, Bogaard HJ, Mizuno S, Clifton B, Xie B, Gao Y, et al. Molecular signature of a right heart failure program in chronic severe pulmonary hypertension. *Am J Respir Cell Mol Biol.* 2011;45(6):1239-47.
14. Gao Z, Xu H, DiSilvestre D, Halperin VL, Tunin R, Tian Y, et al. Transcriptomic profiling of the canine tachycardia-induced heart failure model: global comparison to human and murine heart failure. *J Mol Cell Cardiol.* 2006;40(1):76-86.
15. Potus F, Hindmarch CCT, Dunham-Snary KJ, Stafford J, and Archer SL. Transcriptomic Signature of Right Ventricular Failure in Experimental Pulmonary Arterial Hypertension: Deep Sequencing Demonstrates Mitochondrial, Fibrotic, Inflammatory and Angiogenic Abnormalities. *Int J Mol Sci.* 2018;19(9).
16. Reddy S, Zhao M, Hu DQ, Fajardo G, Katznelson E, Punn R, et al. Physiologic and molecular characterization of a murine model of right ventricular volume overload. *Am J Physiol Heart Circ Physiol.* 2013;304(10):H1314-27.
17. Urashima T, Zhao M, Wagner R, Fajardo G, Farahani S, Quertermous T, et al. Molecular and physiological characterization of RV remodeling in a murine model of pulmonary stenosis. *Am J Physiol Heart Circ Physiol.* 2008;295(3):H1351-H68.
18. di Salvo TG, Yang KC, Brittain E, Absi T, Maltais S, and Hemnes A. Right ventricular myocardial biomarkers in human heart failure. *J Card Fail.* 2015;21(5):398-411.
19. Di Salvo TG, Guo Y, Su YR, Clark T, Brittain E, Absi T, et al. Right ventricular long noncoding RNA expression in human heart failure. *Pulm Circ.* 2015;5(1):135-61.

20. Williams JL, Cavus O, Loccoch EC, Adelman S, Daugherty JC, Smith SA, et al. Defining the molecular signatures of human right heart failure. *Life Sci.* 2018;196:118-26.
21. Khatri P, Sirota M, and Butte AJ. Ten years of pathway analysis: current approaches and outstanding challenges. *PLoS Comput Biol.* 2012;8(2):e1002375.
22. Langfelder P, and Horvath S. WGCNA: an R package for weighted correlation network analysis. *BMC Bioinformatics.* 2008;9:559.
23. Aguero J, Ishikawa K, Hadri L, Santos-Gallego C, Fish K, Hammoudi N, et al. Characterization of right ventricular remodeling and failure in a chronic pulmonary hypertension model. *Am J Physiol Heart Circ Physiol.* 2014;307(8):H1204-15.
24. Gregori M, Tocci G, Giammarioli B, Befani A, Ciavarella GM, Ferrucci A, et al. Abnormal regulation of renin angiotensin aldosterone system is associated with right ventricular dysfunction in hypertension. *Can J Cardiol.* 2014;30(2):188-94.
25. Safdar Z, Thakur A, Singh S, Ji Y, Guffey D, Minard CG, et al. Circulating Aldosterone Levels and Disease Severity in Pulmonary Arterial Hypertension. *J Pulm Respir Med.* 2015;5(5).
26. Maron BA, Opotowsky AR, Landzberg MJ, Loscalzo J, Waxman AB, and Leopold JA. Plasma aldosterone levels are elevated in patients with pulmonary arterial hypertension in the absence of left ventricular heart failure: a pilot study. *Eur J Heart Fail.* 2013;15(3):277-83.
27. Mleczak A, Millar S, Tooze SA, Olson MF, and Chan EY. Regulation of autophagosome formation by Rho kinase. *Cell Signal.* 2013;25(1):1-11.
28. Tsuyuki S, Takabayashi M, Kawazu M, Kudo K, Watanabe A, Nagata Y, et al. Detection of WIPI1 mRNA as an indicator of autophagosome formation. *Autophagy.* 2014;10(3):497-513.
29. Tanida I, Ueno T, and Kominami E. LC3 and Autophagy. *Methods Mol Biol.* 2008;445:77-88.
30. Qian J, Ren X, Wang X, Zhang P, Jones WK, Molkentin JD, et al. Blockade of Hsp20 phosphorylation exacerbates cardiac ischemia/reperfusion injury by suppressed autophagy and increased cell death. *Circulation research.* 2009;105(12):1223-31.
31. Codogno P, Mehrpour M, and Proikas-Cezanne T. Canonical and non-canonical autophagy: variations on a common theme of self-eating? *Nat Rev Mol Cell Biol.* 2012;13(1):7-12.
32. Lazarou M, Sliter DA, Kane LA, Sarraf SA, Wang C, Burman JL, et al. The ubiquitin kinase PINK1 recruits autophagy receptors to induce mitophagy. *Nature.* 2015;524(7565):309-14.
33. Florey O, Gammoh N, Kim SE, Jiang X, and Overholtzer M. V-ATPase and osmotic imbalances activate endolysosomal LC3 lipidation. *Autophagy.* 2015;11(1):88-99.
34. Martinez-Martin N, Maldonado P, Gasparini F, Frederico B, Aggarwal S, Gaya M, et al. A switch from canonical to noncanonical autophagy shapes B cell responses. *Science.* 2017;355(6325):641-7.
35. Dai DF, Johnson SC, Villarin JJ, Chin MT, Nieves-Cintrón M, Chen T, et al. Mitochondrial oxidative stress mediates angiotensin II-induced cardiac hypertrophy and Galphaq overexpression-induced heart failure. *Circulation research.* 2011;108(7):837-46.
36. Lee J, Giordano S, and Zhang J. Autophagy, mitochondria and oxidative stress: cross-talk and redox signalling. *Biochem J.* 2012;441(2):523-40.
37. Proikas-Cezanne T, Takacs Z, Donnes P, and Kohlbacher O. WIPI proteins: essential PtdIns3P effectors at the nascent autophagosome. *J Cell Sci.* 2015;128(2):207-17.
38. Hein S, Arnon E, Kostin S, Schonburg M, Elsasser A, Polyakova V, et al. Progression from compensated hypertrophy to failure in the pressure-overloaded human heart: structural deterioration and compensatory mechanisms. *Circulation.* 2003;107(7):984-91.
39. Kostin S, Pool L, Elsasser A, Hein S, Drexler HC, Arnon E, et al. Myocytes die by multiple mechanisms in failing human hearts. *Circulation research.* 2003;92(7):715-24.
40. Matsui Y, Takagi H, Qu X, Abdellatif M, Sakoda H, Asano T, et al. Distinct roles of autophagy in the heart during ischemia and reperfusion: roles of AMP-activated protein kinase and Beclin 1 in mediating autophagy. *Circulation research.* 2007;100(6):914-22.
41. Nakai A, Yamaguchi O, Takeda T, Higuchi Y, Hikoso S, Taniike M, et al. The role of autophagy in cardiomyocytes in the basal state and in response to hemodynamic stress. *Nat Med.* 2007;13(5):619-24.
42. Xu X, Kobayashi S, Chen K, Timm D, Volden P, Huang Y, et al. Diminished autophagy limits cardiac injury in mouse models of type 1 diabetes. *J Biol Chem.* 2013;288(25):18077-92.
43. Zhu H, Tannous P, Johnstone JL, Kong Y, Shelton JM, Richardson JA, et al. Cardiac autophagy is a maladaptive response to hemodynamic stress. *J Clin Invest.* 2007;117(7):1782-93.

44. Shirakabe A, Zhai P, Ikeda Y, Saito T, Maejima Y, Hsu CP, et al. Drp1-Dependent Mitochondrial Autophagy Plays a Protective Role Against Pressure Overload-Induced Mitochondrial Dysfunction and Heart Failure. *Circulation*. 2016;133(13):1249-63.
45. Ucar A, Gupta SK, Fiedler J, Erikci E, Kardasinski M, Batkai S, et al. The miRNA-212/132 family regulates both cardiac hypertrophy and cardiomyocyte autophagy. *Nat Commun*. 2012;3:1078.
46. Wu P, Yuan X, Li F, Zhang J, Zhu W, Wei M, et al. Myocardial Upregulation of Cathepsin D by Ischemic Heart Disease Promotes Autophagic Flux and Protects Against Cardiac Remodeling and Heart Failure. *Circ Heart Fail*. 2017;10(7).
47. Schluter KD, Kutsche HS, Hirschhauser C, Schreckenberger R, and Schulz R. Review on Chamber-Specific Differences in Right and Left Heart Reactive Oxygen Species Handling. *Front Physiol*. 2018;9:1799.
48. Cheng G, Takahashi M, Shunmugavel A, Wallenborn JG, DePaoli-Roach AA, Gergs U, et al. Basis for MAP4 dephosphorylation-related microtubule network densification in pressure overload cardiac hypertrophy. *J Biol Chem*. 2010;285(49):38125-40.
49. Fassett JT, Hu X, Xu X, Lu Z, Zhang P, Chen Y, et al. AMPK attenuates microtubule proliferation in cardiac hypertrophy. *Am J Physiol Heart Circ Physiol*. 2013;304(5):H749-58.
50. Mogessie B, Roth D, Rahil Z, and Straube A. A novel isoform of MAP4 organises the paraxial microtubule array required for muscle cell differentiation. *Elife*. 2015;4:e05697.
51. Teng M, Dang YM, Zhang JP, Zhang Q, Fang YD, Ren J, et al. Microtubular stability affects cardiomyocyte glycolysis by HIF-1 α expression and endonuclear aggregation during early stages of hypoxia. *Am J Physiol Heart Circ Physiol*. 2010;298(6):H1919-31.
52. Scholz D, McDermott P, Garnovskaya M, Gallien TN, Huettelmaier S, DeRienzo C, et al. Microtubule-associated protein-4 (MAP-4) inhibits microtubule-dependent distribution of mRNA in isolated neonatal cardiocytes. *Cardiovasc Res*. 2006;71(3):506-16.
53. Takahashi M, Shiraishi H, Ishibashi Y, Blade KL, McDermott PJ, Menick DR, et al. Phenotypic consequences of beta1-tubulin expression and MAP4 decoration of microtubules in adult cardiocytes. *Am J Physiol Heart Circ Physiol*. 2003;285(5):H2072-83.
54. Chu G, Egnaczyk GF, Zhao W, Jo SH, Fan GC, Maggio JE, et al. Phosphoproteome analysis of cardiomyocytes subjected to beta-adrenergic stimulation: identification and characterization of a cardiac heat shock protein p20. *Circulation research*. 2004;94(2):184-93.
55. Pipkin W, Johnson JA, Creazzo TL, Burch J, Komalavilas P, and Brophy C. Localization, macromolecular associations, and function of the small heat shock-related protein HSP20 in rat heart. *Circulation*. 2003;107(3):469-76.
56. Wang X, Zingarelli B, O'Connor M, Zhang P, Adeyemo A, Kranias EG, et al. Overexpression of Hsp20 prevents endotoxin-induced myocardial dysfunction and apoptosis via inhibition of NF-kappaB activation. *J Mol Cell Cardiol*. 2009;47(3):382-90.
57. Liu GS, Zhu H, Cai WF, Wang X, Jiang M, Essandoh K, et al. Regulation of BECN1-mediated autophagy by HSPB6: Insights from a human HSPB6(S10F) mutant. *Autophagy*. 2018;14(1):80-97.
58. Fan GC, Ren X, Qian J, Yuan Q, Nicolaou P, Wang Y, et al. Novel cardioprotective role of a small heat-shock protein, Hsp20, against ischemia/reperfusion injury. *Circulation*. 2005;111(14):1792-9.
59. Horvath S, Zhang B, Carlson M, Lu KV, Zhu S, Felciano RM, et al. Analysis of oncogenic signaling networks in glioblastoma identifies ASPM as a molecular target. *Proc Natl Acad Sci U S A*. 2006;103(46):17402-7.
60. Xue Z, Huang K, Cai C, Cai L, Jiang CY, Feng Y, et al. Genetic programs in human and mouse early embryos revealed by single-cell RNA sequencing. *Nature*. 2013;500(7464):593-7.
61. Liu Q, Jiang C, Xu J, Zhao MT, Van Bortle K, Cheng X, et al. Genome-Wide Temporal Profiling of Transcriptome and Open Chromatin of Early Cardiomyocyte Differentiation Derived From hiPSCs and hESCs. *Circulation research*. 2017;121(4):376-91.
62. Thenappan T, Prins KW, Pritzker MR, Scandurra J, Volmers K, and Weir EK. The Critical Role of Pulmonary Arterial Compliance in Pulmonary Hypertension. *Ann Am Thorac Soc*. 2016;13(2):276-84.
63. Redout EM, Wagner MJ, Zuidwijk MJ, Boer C, Musters RJ, van Hardeveld C, et al. Right-ventricular failure is associated with increased mitochondrial complex II activity and production of reactive oxygen species. *Cardiovasc Res*. 2007;75(4):770-81.
64. Dipla K, Mattiello JA, Jeevanandam V, Houser SR, and Margulies KB. Myocyte recovery after mechanical circulatory support in humans with end-stage heart failure. *Circulation*. 1998;97(23):2316-22.

65. Atluri P, Goldstone AB, Fairman AS, MacArthur JW, Shudo Y, Cohen JE, et al. Predicting right ventricular failure in the modern, continuous flow left ventricular assist device era. *Ann Thorac Surg*. 2013;96(3):857-63; discussion 63-4.
66. Ben-Ari Fuchs S, Lieder I, Stelzer G, Mazor Y, Buzhor E, Kaplan S, et al. GeneAnalytics: An Integrative Gene Set Analysis Tool for Next Generation Sequencing, RNAseq and Microarray Data. *OMICS*. 2016;20(3):139-51.
67. Assenov Y, Ramirez F, Schelhorn SE, Lengauer T, and Albrecht M. Computing topological parameters of biological networks. *Bioinformatics*. 2008;24(2):282-4.
68. Csardi G, and Nepusz T. The igraph software package for complex network research. <http://igraph.org>. Updated 2006 Accessed 1695.
69. Fagerberg L, Hallstrom BM, Oksvold P, Kampf C, Djureinovic D, Odeberg J, et al. Analysis of the human tissue-specific expression by genome-wide integration of transcriptomics and antibody-based proteomics. *Mol Cell Proteomics*. 2014;13(2):397-406.
70. Shannon P, Markiel A, Ozier O, Baliga NS, Wang JT, Ramage D, et al. Cytoscape: a software environment for integrated models of biomolecular interaction networks. *Genome Res*. 2003;13(11):2498-504.
71. Warnes GR, Bolker B, Bonebakker L, Gentleman R, Huber W, Liaw A, et al. gplots: Various R Programming Tools for Plotting Data. R package version 3.0.1. 2016:<https://CRAN.R-project.org/package=gplots>.
72. Rockman HA, Ross RS, Harris AN, Knowlton KU, Steinhilper ME, Field LJ, et al. Segregation of atrial-specific and inducible expression of an atrial natriuretic factor transgene in an in vivo murine model of cardiac hypertrophy. *Proc Natl Acad Sci U S A*. 1991;88(18):8277-81.
73. Rockman HA, Ono S, Ross RS, Jones LR, Karimi M, Bhargava V, et al. Molecular and physiological alterations in murine ventricular dysfunction. *Proc Natl Acad Sci U S A*. 1994;91(7):2694-8.
74. Georgakopoulos D, Mitzner WA, Chen CH, Byrne BJ, Millar HD, Hare JM, et al. In vivo murine left ventricular pressure-volume relations by miniaturized conductance micromanometry. *Am J Physiol*. 1998;274(4 Pt 2):H1416-22.
75. Simpson P, and Savion S. Differentiation of rat myocytes in single cell cultures with and without proliferating nonmyocardial cells. Cross-striations, ultrastructure, and chronotropic response to isoproterenol. *Circulation research*. 1982;50(1):101-16.
76. Folda A, Citta A, Scalcon V, Cali T, Zonta F, Scutari G, et al. Mitochondrial Thioredoxin System as a Modulator of Cyclophilin D Redox State. *Sci Rep*. 2016;6:23071.

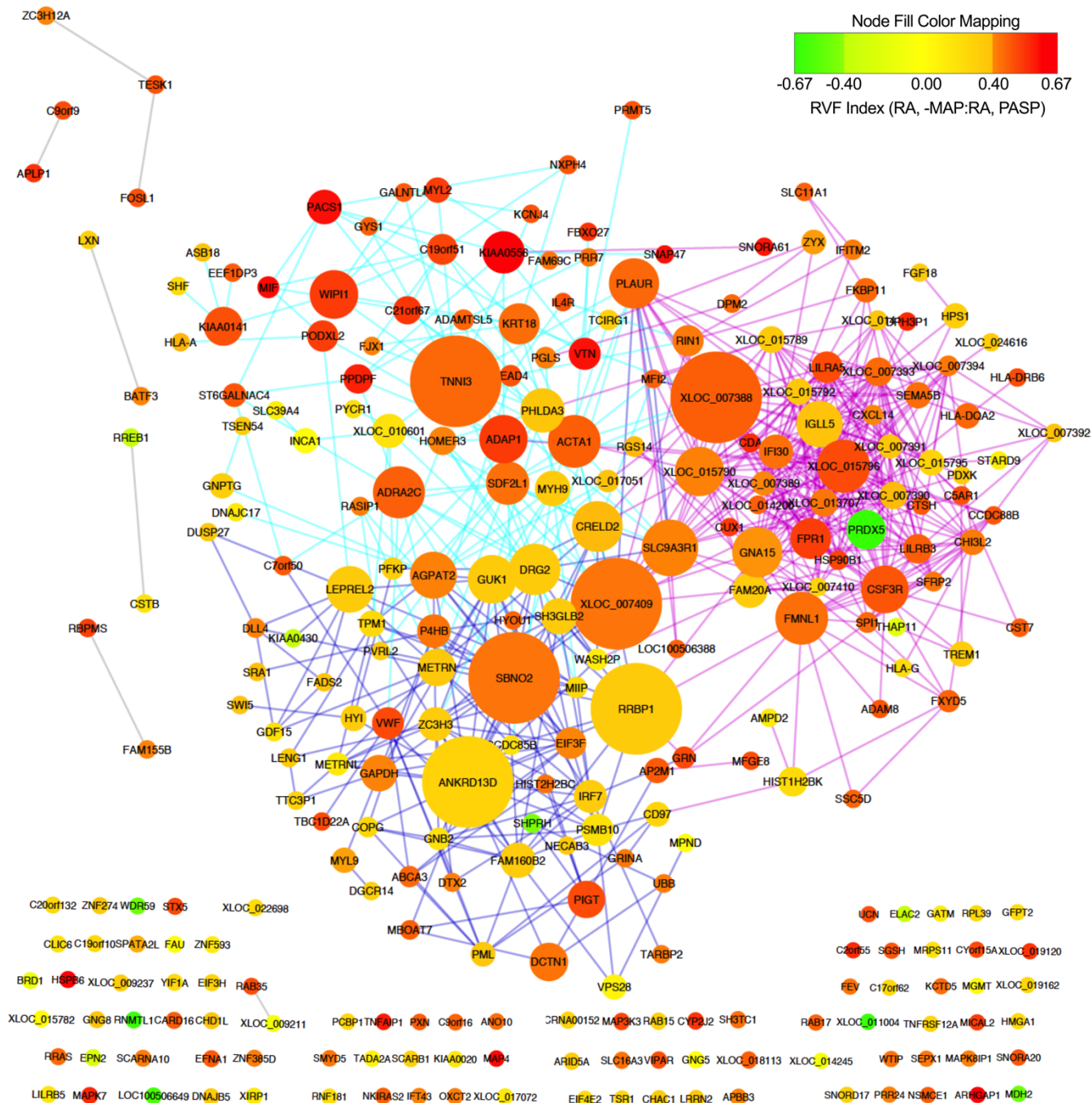


Figure 1. Visualization of lightgreen module correlated with composite right ventricular failure (RVF) index. All members of the lightgreen module are connected at a co-expression correlation threshold of 0.667. The module network is filtered to show edges between transcript pairs with a co-expression correlation value ≥ 0.88 . Gene set pathway analysis revealed a trilobar structure with signaling themes. Cyan edges delineate the “Cardiac Signaling Lobe”; purple edges delineate the “Innate Immunity Lobe”, and dark blue edges delineate the “Intracellular Signaling Lobe”. Node size reflects the betweenness centrality of the transcript; the larger the node size, the greater the betweenness centrality. Each node is also correlated to a composite index of hemodynamic parameters associated with RVF— right atrial pressure (RA), mean arterial pressure to right atrial pressure ratio (MAP:RA), and pulmonary artery systolic pressure (PASP). Positive correlations between transcript node and composite RVF index are represented in orange to red, thereby designating “drivers” of RVF. Negative correlations between transcript node and composite RVF index are represented in green, thereby designating “repressors” of RVF.

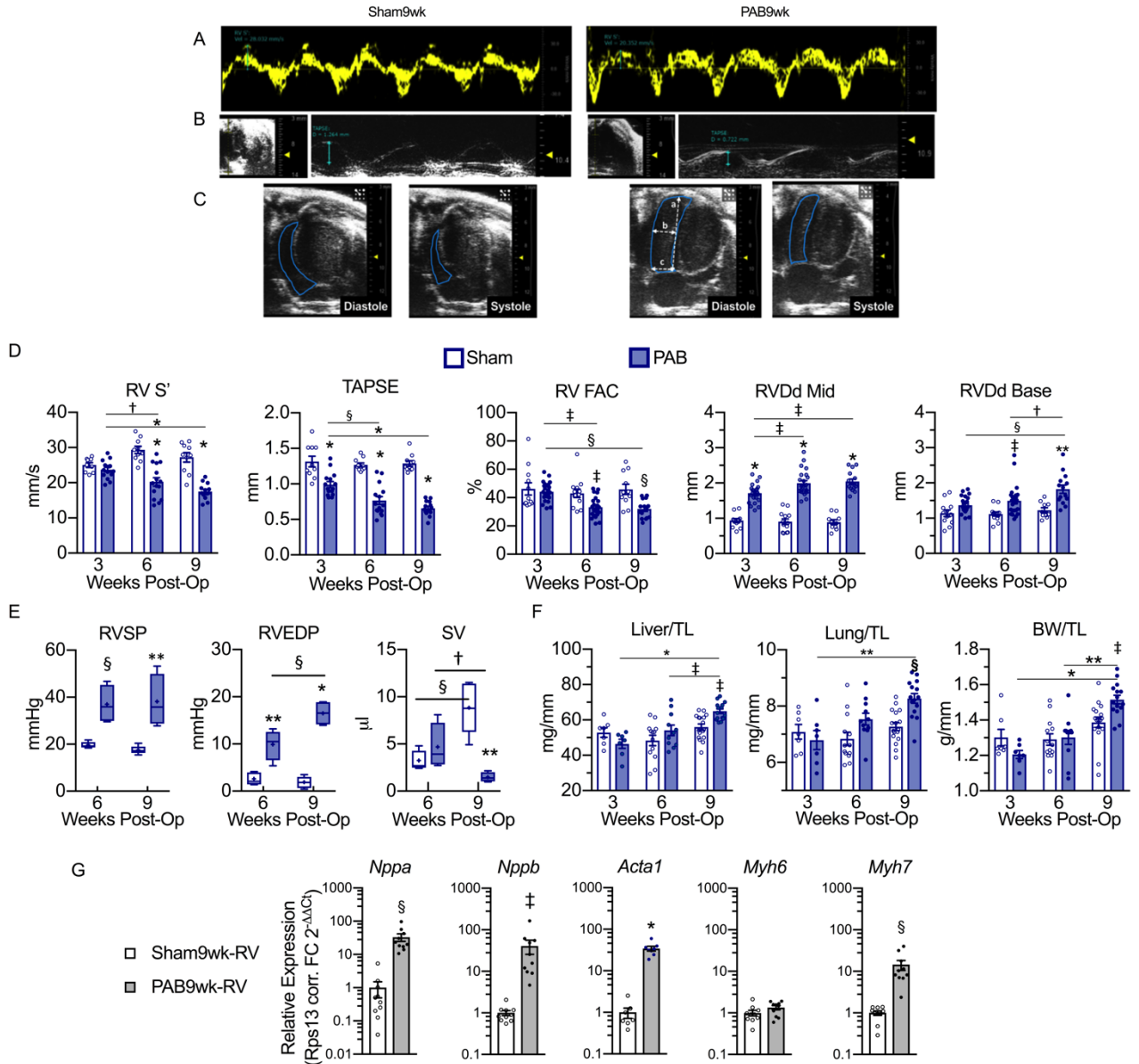


Figure 2. Pulmonary artery banding (PAB) induces progressive dilatation, functional decline, and eventual failure of the right ventricle (RV) over a 9 wk course. C57BL/6J WT male mice were subjected to Sham or PAB surgery and assessed at 3 wk intervals, up to 9 wk post-surgery. Representative echocardiographic images of: **(A)** tissue doppler assessment of RV systolic function by lateral tricuspid annular systolic velocity S'; **(B)** M-mode assessment of TAPSE (tricuspid annulus planar systolic excursion); **(C)** B-mode assessment of RV FAC (fractional area change) and RV diastolic dimensions (a, major axis dimension; b, mid-cavity dimension; c, basal dimension). **(D)** Summary of echocardiographic assessment of RV function and structure, $n = 10-15$ per group; **(E)** Terminal hemodynamic assessment of RV pressures (RVSP, RV peak systolic pressure; RVEDP, RV end-diastolic pressure) and stroke volume (SV) at 6- and 9-wk post-surgery for PAB and Sham mice, $n=5$ per Sham group, $n=4$ per PAB group; **(F)** Morphometric assessment of hepatic congestion (Liver/TL, liver weight/tibia length), pulmonary edema (Lung/TL, lung weight/tibia length), and peripheral edema (BW/TL), $n = 7-17$ per group; **(G)** RT-qPCR analysis of fetal gene program in RV myocardium of PAB9wk versus Sham9wk, $n=7-10$ per group. * $p<0.0001$, † $p<0.1$, § $p<0.01$, ‡ $p<0.05$, ** $p<0.001$ vs respective Sham unless otherwise indicated by comparison bar, on Tukey's multiple comparison testing following two-way ANOVA for panels D-F; on two-tailed, unpaired Student's t-test for panel G. Scatter dot plots with bars show individual values and mean±SEM. Box-whisker plots show mean (+), median (midline), 25th and 75th percentiles (box), minimum, and maximum values.

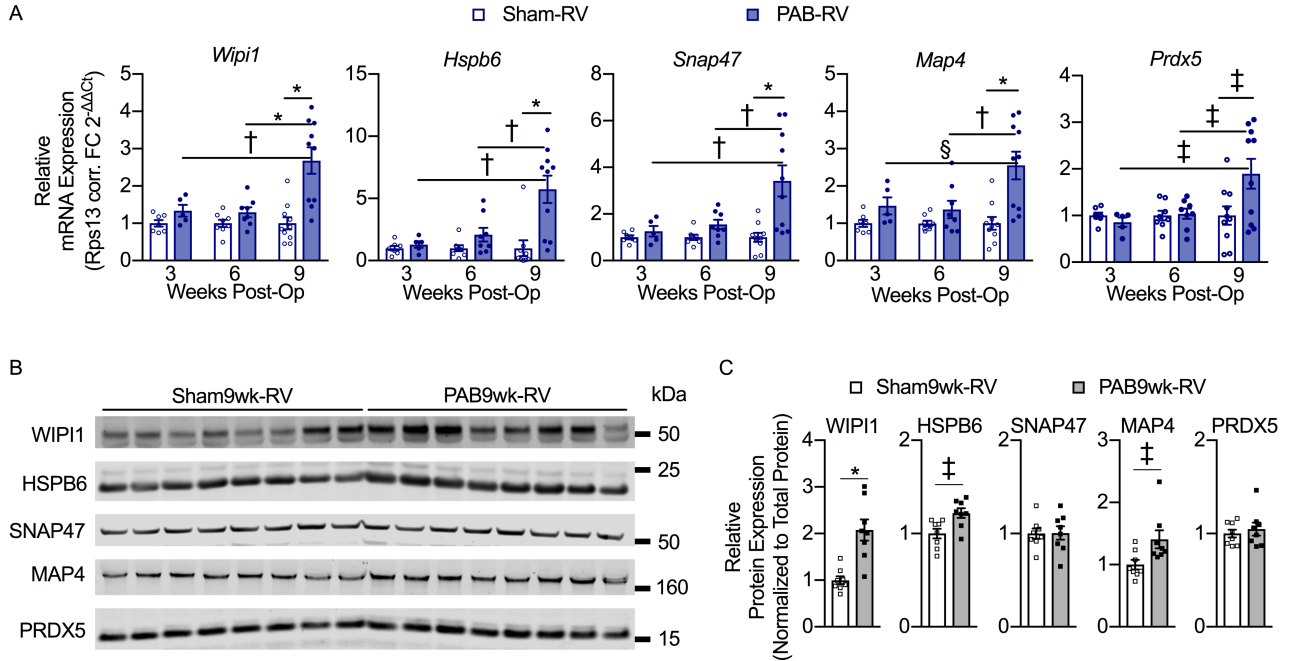


Figure 3. Transcript and protein expression of WGCNA identified, RVF-associated gene hub, drivers, and repressor in pulmonary artery banding (PAB) mouse model. RNA and protein were extracted from the RV of C57BL/6J WT male mice subjected to Sham or PAB. **(A)** RT-qPCR analysis of *Wipi1*, *Hspb6*, *Snap47*, *Map4*, and *Prdx5* in RV of Sham and PAB mice at 3-, 6-, and 9-wk post-surgery; **(B)** Representative Western blots; and **(C)** Summary densitometry analysis of Westerns, normalized to total protein stain, relative to Sham control. Total protein stain not shown. * $p < 0.001$, † $p < 0.01$, ‡ $p < 0.05$, § $p = 0.06$ on Tukey's multiple comparison testing following two-way ANOVA for panel A; on two-tailed, unpaired Student's t-test for panel C. $n = 5-10$ per group. Scatter dot plots with bars show individual values and mean \pm SEM.

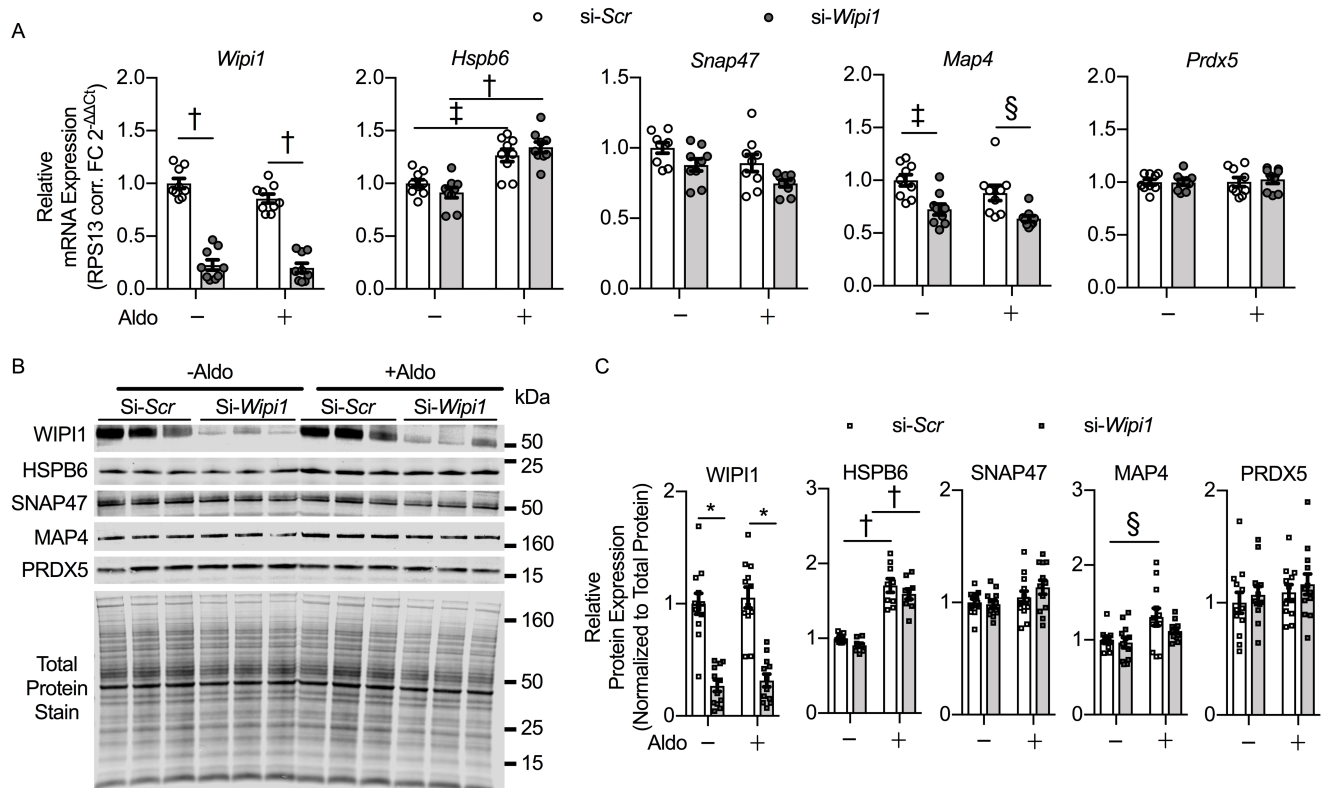


Figure 4. Effect of silencing *Wipi1* on hub, drivers, and repressor of WGCNA identified right ventricular failure (RVF)-associated module. Neonatal rat ventricular myocytes (NRVMs) were transfected with scramble or *Wipi1*-specific siRNAs and then stimulated with aldosterone (Aldo, $1\mu\text{M}$) for 48h. **(A)** Effect of Aldo stimulation and *Wipi1* silencing on transcript levels of WGCNA identified RVF-associated genetic hub, drivers, and repressor ($n=9$ per group from 3 independent experiments). **(B)** Representative Western blot. **(C)** Summary of Western analysis ($n=9-12$ per group from 3-4 independent experiments). * $p<0.001$, † $p<0.0001$, ‡ $p<0.01$, § $p<0.05$ on Tukey's multiple comparison testing following two-way ANOVA. Scatter dot plots with bars show individual values and mean \pm SEM.

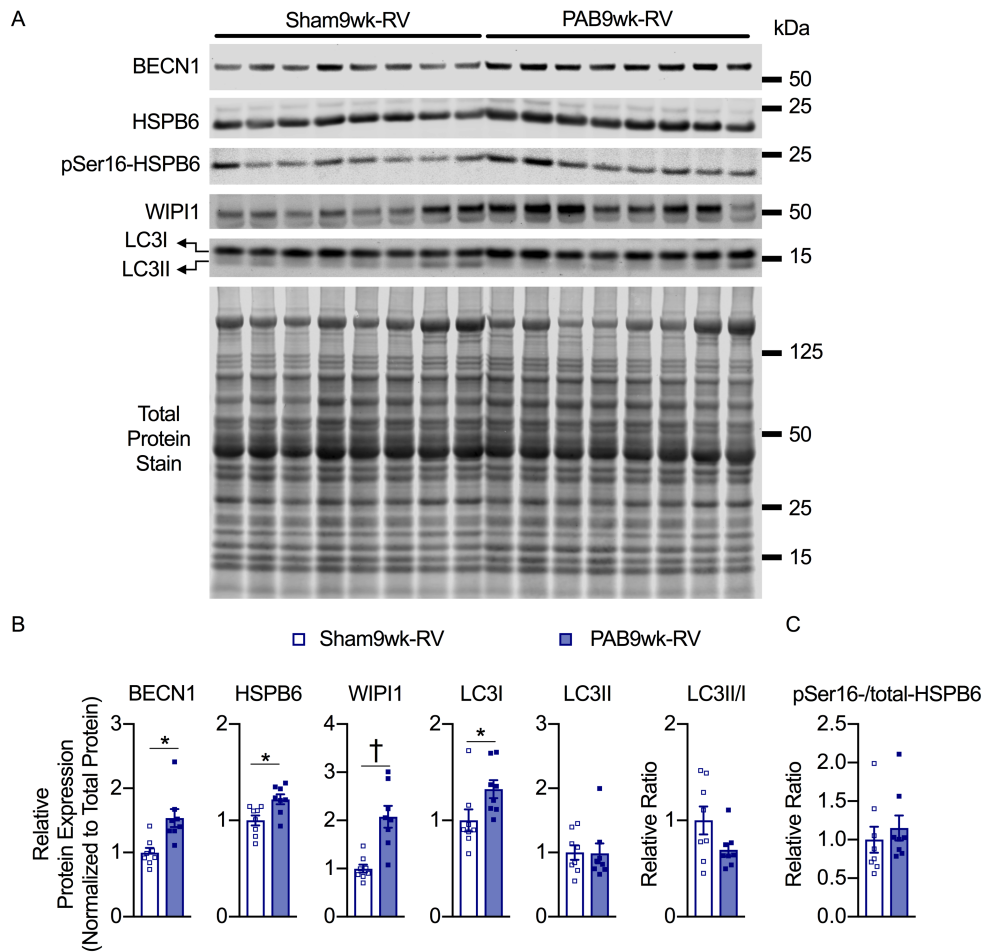


Figure 5. Non-canonical autophagy is upregulated in the failing right ventricle (RV) of pulmonary artery banding (PAB) mouse model. Protein lysates were prepared from RV of 9wk Sham or PAB operated C57BL/6J WT male mice. **(A)** Western blots of autophagy proteins and total protein stain in non-failing Sham9wk-RV and failing PAB9wk-RV. The HSPB6 and WIP11 blots shown are reused from Figure 3B. **(B)** Summary of Western analyses reveals upregulation of BECN1, HSPB6, WIP11, and non-lipidated LC3 (LC3I) without an increase in either LC3 lipidation (LC3II and LC3II/I ratio) or **(C)** Ser16 phosphorylation of HSPB6 in failing PAB9wk-RV versus non-failing Sham9wk-RV. This suggests a shift towards non-canonical autophagy pathways in the failing RV. * $p < 0.05$, † $p < 0.001$ on two-tailed Student's t-test; $n = 8$ per group. Scatter dot plots with bars show individual values and mean \pm SEM.

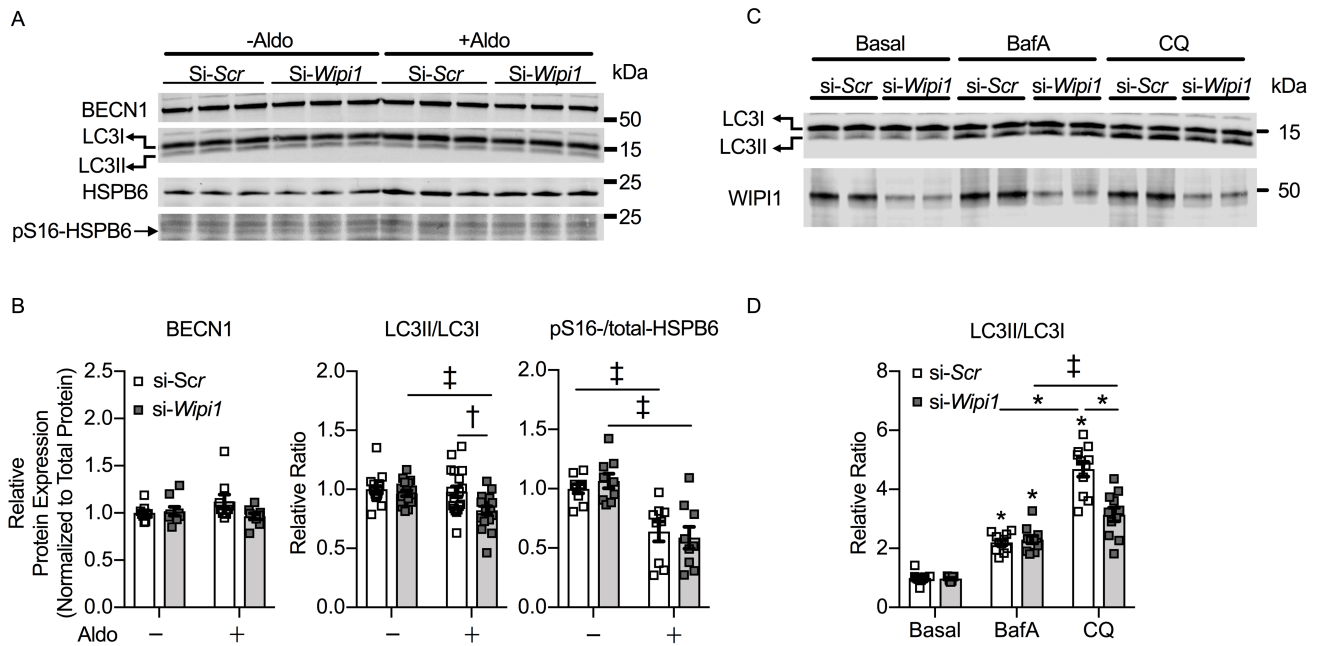


Figure 6. Silencing *Wipi1* blunts aldosterone induction of non-canonical autophagy. Neonatal rat ventricular myocytes (NRVMs) were transfected with scramble or *Wipi1*-specific siRNAs and then stimulated with aldosterone (Aldo, 1 μ M, 48h), bafilomycin A (BafA, 100nM, 1h), or chloroquine (CQ, 100 μ M, 1h). **(A)** Representative Western blots of autophagy proteins (n=9-18 per group from 3-6 independent experiments). **(B)** Summary Western analysis of LC3 lipidation (LC3II/LC3I) and canonical autophagy (pS16-/total HSPB6). **(C)** Representative Western blots of LC3 and WIP1 in si-scramble versus si-*Wipi1* transfected NRVMs treated with BafA or CQ to differentiate, respectively, canonical versus non-canonical autophagy. BafA blocks LCII lysosomal degradation during canonical autophagy, whereas CQ inhibits the fusion between the autophagosome and lysosome. Hence, CQ reveals total autophagic flux and the difference between the effects of CQ and BafA on LC3II/I ratios is attributable to non-canonical autophagy (32, 33). **(D)** Quantification of LC3II/I ratio show that silencing *Wipi1* selectively inhibits non-canonical autophagy (CQ) without affecting canonical autophagy (BafA) ($n=11$ per group from 4 independent experiments for LC3II/I). * $p<0.0001$, ‡ $p<0.01$, † $p<0.05$ versus basal, unless otherwise indicated by comparison bar, on Tukey's multiple comparison test following two-way ANOVA. Scatter dot plots with bars show individual values and mean \pm SEM.

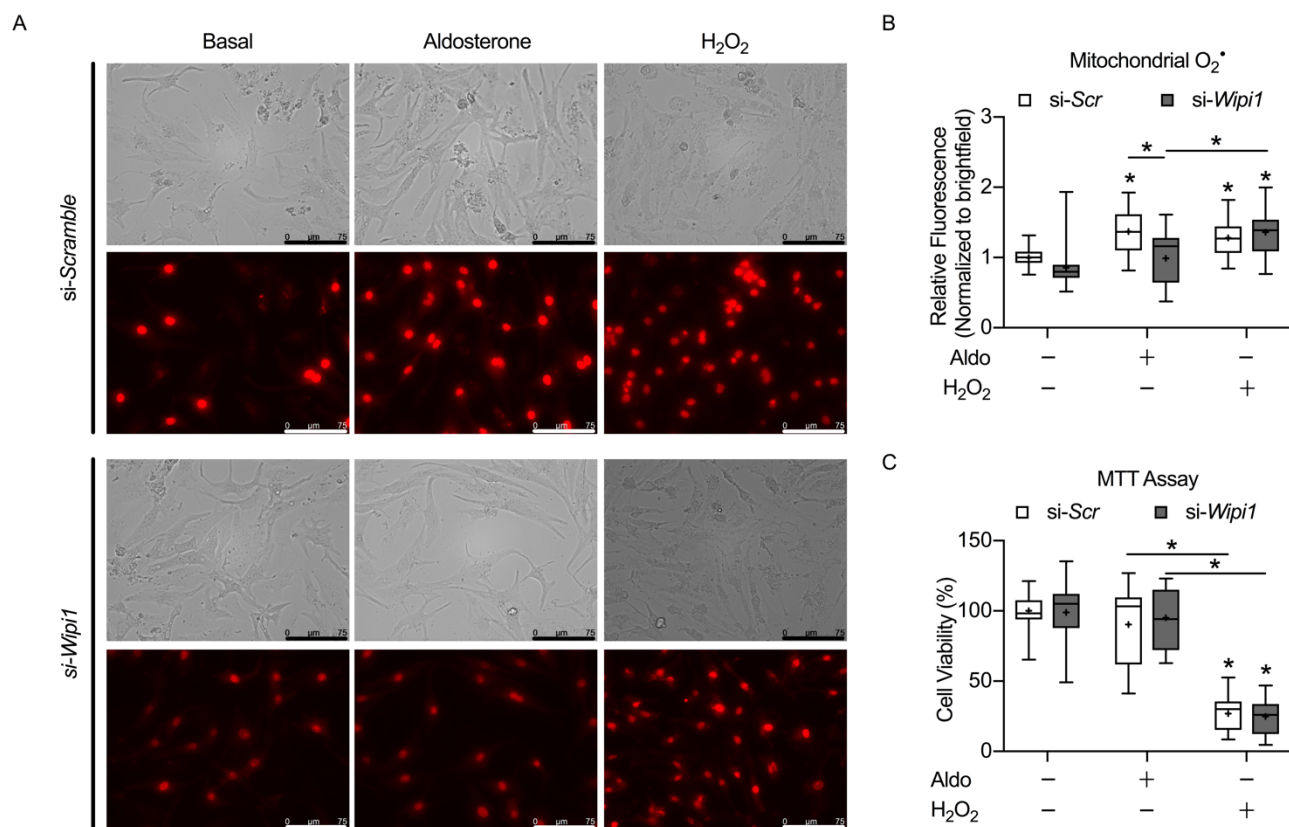


Figure 7. Silencing *Wipi1* decreases mitochondrial superoxide (O₂[•]) levels in *in vitro* neuro-hormonal model of right ventricular failure (RVF). Neonatal rat ventricular myocytes (NRVMs) were transfected with scramble or *Wipi1*-specific siRNAs and then stimulated with aldosterone (Aldo, 1 μ M, 48h) or hydrogen peroxide (H₂O₂, 50 μ M, 2h). **(A)** Brightfield and MitoSOX red imaging of NRVMs transfected with si-scramble versus si-*Wipi1*, with and without aldosterone (Aldo) stimulation. H₂O₂ was used as a positive control. ($n=39-44$ per group from 6 independent experiments). Scale bar measures 75 μ M. **(B)** Summary analysis of mitochondrial O₂[•] levels ($n=41-44$ per group from 6 independent experiments). **(C)** Cell viability as assessed by MTT assay ($n=24$ per group from 3 independent experiments). * $p<0.0001$ versus respective unstimulated baseline unless indicated otherwise by comparison bar, on Tukey's multiple comparison test following two-way ANOVA. Box and whisker plots show mean (+), median (midline), 25th and 75th percentiles (box), minimum and maximum values (whiskers).

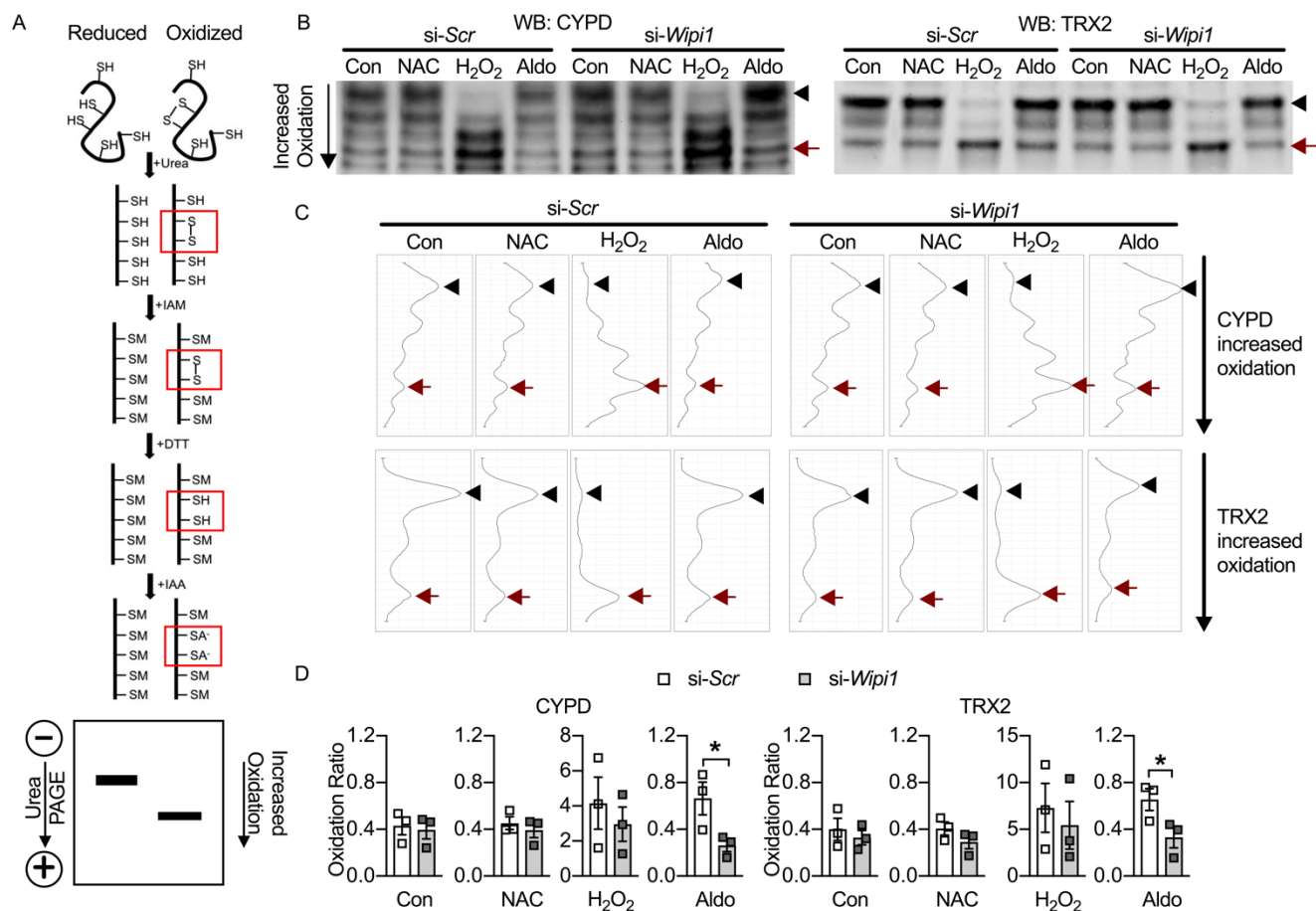


Figure 8. Silencing *Wipi1* mitigates aldosterone induced oxidation of mitochondrial proteins CYPD and TRX2. Neonatal rat ventricular myocytes (NRVMs) were treated with oxidizing or reducing agents and then subjected to urea lysis, iodoacetamide-iodoacetic acid (IAM-IAA) alkylation, and Western analysis. **(A)** Schematic representation of the IAM-IAA alkylation method for identifying oxidized and reduced proteins in native non-reducing urea PAGE. **(B)** Representative redox Western blots for CYPD and TRX2 of NRVMs treated with: 1) Control, 2) reducing agent N-acetyl cysteine (NAC), 3) oxidizing agent hydrogen peroxide (H₂O₂), 4) aldosterone (Aldo). Black arrowhead, reduced protein band. Red arrow, oxidized protein band. **(C)** Histogram of Western densitometry analysis of CYPD and TRX2 oxidation. **(D)** Quantification of CYPD and TRX2 oxidation under different redox conditions as shown by the ratio of oxidized to reduced protein band signals ($n=3$ per group). * $p<0.05$ on one-tailed Student's t-test; Scatter dot plots with bars show individual values and mean \pm SEM.

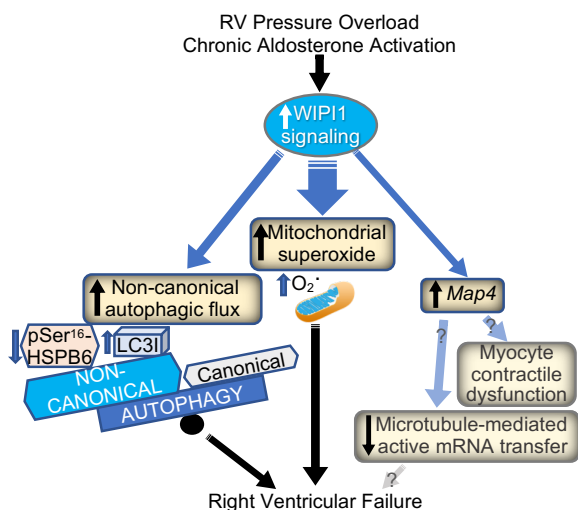


Figure 9. Proposed schematic of *Wipi1* signaling mechanisms underlying right ventricular failure (RVF). RV pressure overload and chronic aldosterone activation upregulate WIP1 signaling in the failing RV. Enhanced WIP1 signaling increases mitochondrial superoxide levels and non-canonical autophagic flux. *WIP1* upregulation also correlates with increased *Map4* expression, thereby potentially triggering MAP4-mediated myocyte contractile dysfunction or inhibition of microtubule-mediated active mRNA transfer. In vitro studies in neonatal rat ventricular myocytes demonstrated the feasibility of mitigating aldosterone-induced mitochondrial superoxide levels, blunting non-canonical autophagy, and decreasing *Map4* expression by silencing *Wipi1*. Further studies are warranted to elucidate mechanistic details of WIP1 signaling and to confirm the therapeutic potential of targeting WIP1 in RVF.

Gene	Correlation Coefficient (Pearson's <i>p</i> value)						RVF Index
	RA	RA:PCWP	MAP:RA	PASP	SBP	CI	
HSPB6	0.810 (<0.001)	0.803 (<0.001)	-0.583 (0.023)	0.861 (<0.001)	-0.642 (0.010)	-0.688 (0.005)	0.75
SNAP47	0.735 (0.002)	0.727 (0.002)	-0.689 (0.005)	0.686 (0.005)	-0.761 (0.001)	-0.575 (0.025)	0.70
MAP4	0.703 (0.003)	0.592 (0.020)	-0.500 (0.058)	0.746 (0.001)	-0.697 (0.004)	-0.624 (0.013)	0.65
PRDX5	-0.679 (0.009)	-0.660 (0.007)	0.600 (0.019)	-0.630 (0.012)	0.602 (0.018)	0.745 (0.001)	-0.64
WIP1	0.528 (0.043)	0.477 (0.072)	-0.455 (0.088)	0.664 (0.007)	-0.624 (0.013)	-0.442 (0.099)	0.55

Table 1. Pearson's correlation coefficients of RVF-associated drivers, repressor, and hub with hemodynamic indices. RA, right atrial pressure; RA:PCWP, ratio of right atrial pressure to pulmonary capillary wedge pressure; MAP:RA, ratio of mean arterial pressure to right atrial pressure; PASP, pulmonary artery systolic pressure; SBP, systolic blood pressure; CI, cardiac index; RVF, right ventricular failure; RVF index is calculated as the average of three coefficients---- the correlation coefficients for RA and PASP and the negative value of the correlation coefficient for MAP:RA. Pearson's *p* values are presented in parentheses.